



Understanding the Planetary Formation and Evolution in Star Clusters (UPiC). I. Evidence of Hot Giant Exoplanets Formation Timescales

Yuan-Zhe Dai^{1,2} , Hui-Gen Liu^{1,2} , Jia-Yi Yang^{1,2} , and Ji-Lin Zhou^{1,2} ¹ School of Astronomy and Space Science, Nanjing University, 163 Xianlin Avenue, Nanjing, 210023, People's Republic of China; huigen@nju.edu.cn² Key Laboratory of Modern Astronomy and Astrophysics, Ministry of Education, Nanjing, 210023, People's Republic of China

Received 2023 June 4; revised 2023 September 5; accepted 2023 September 25; published 2023 November 2

Abstract

Planets in young star clusters could shed light on planet formation and evolution since star clusters can provide accurate age estimation. However, the number of transiting planets detected in clusters was only ~ 30 , too small for statistical analysis. Thanks to the unprecedented high-precision astrometric data provided by Gaia DR2 and Gaia DR3, many new open clusters (OCs) and comoving groups have been identified. The Understanding Planetary Formation and Evolution in Star Clusters project aims to find observational evidence and interpret how planets form and evolve in cluster environments. In this work, we cross match the stellar catalogs of new OCs and comoving groups with confirmed planets and candidates. We carefully remove false positives and obtain the biggest catalog of planets in star clusters up to now, which consists of 73 confirmed planets and 84 planet candidates. After age validation, we obtain the radius–age diagram of these planets/candidates. We find an increment in the fraction of hot Jupiters (HJs) around 100 Myr and attribute the increment to the flyby-induced high- e migration in star clusters. An additional small bump of the fraction of HJs after 1 Gyr is detected, which indicates the formation timescale of HJ around field stars is much larger than that in star clusters. Thus, stellar environments play important roles in the formation of HJs. The hot Neptune desert occurs around 100 Myr in our sample. A combination of photoevaporation and high- e migration may sculpt the hot Neptune desert in clusters.

Unified Astronomy Thesaurus concepts: [Exoplanet catalogs \(488\)](#); [Exoplanets \(498\)](#); [Exoplanet evolution \(491\)](#); [Open star clusters \(1160\)](#); [Astrostatistics \(1882\)](#)

Supporting material: machine-readable table

1. Introduction

Open clusters (OCs) in the Milky Way are the collection of stars formed from the same molecular cloud and gravitationally bound together, thus sharing similar specific characteristics, e.g., age, distance, reddening, metal abundance, etc. OCs provide an ideal laboratory for studying star formation and evolution. Recent studies based on Kepler data show that nearly 50% of stars have host planets (Zhu & Dong 2021). Since most stars form in clusters (Lada & Lada 2003), many exoplanets are formed in cluster environments. Therefore, the majority of stars will eventually become field stars as clusters are dissociated. Detecting exoplanets in OCs can provide an ideal sample for studying planet formation and evolution.

The first planet in OCs, ϵ tau b, was detected by Sato et al. (2007) via radial velocity. Kepler-66b and Kepler-67b are the first cluster planets discovered by transit (Meibom et al. 2013). Thanks to Kepler/K2 and TESS, tens of planets in clusters have been discovered, and the number is growing. There are several programs focusing on planets in star clusters, especially young exoplanets. Zodiacal Exoplanets In Time collaboration uses K2 data to monitor young OCs and associations in the ecliptic plane and found planets in the Hyades, Praesepe, Upper Sco, and Taurus (Mann et al. 2016a, 2016b, 2017, 2018; Gaidos et al. 2017; Rizzuto et al. 2017, 2018; Vanderburg et al. 2018). With the help of extensive follow-up observations, the TESS Hunt for Young and Maturing Exoplanets collaboration has reported on

planets in Upper Sco (Rizzuto et al. 2020), the Tucana–Horologium association (Newton et al. 2019), the Ursa Major moving group (Mann et al. 2020), and the Pisces Eridanus stream (Newton et al. 2021). Bouma et al. (2019, 2020) began a Cluster Difference Imaging Photometric Survey to discover giant transiting planets with known ages and to provide lightcurves suitable for studies in stellar astrophysics. Nardiello et al. (2019, 2020, 2021) and Nardiello (2020) use a point-spread function-based Approach to TESS high-quality data of star clusters (PATHOS) and find 90 planet candidates. The GAPS Young Objects project aims to search and characterize young hot Jupiters (HJs) and put constraints on evolutionary models (e.g., Carleo et al. 2020). For planets at larger separations, direct imaging plays an important role. There are dozens of young planets discovered through direct imaging, e.g., 2MASS J12073346-3932539 b (Chauvin et al. 2004), DH Tau b (Itoh et al. 2005), GQ Lup b (Neuhäuser et al. 2005), etc.

Hitherto, there have been many surveys and projects focusing on the young planets in clusters, but the number of reported planets in clusters is limited and is not enough to support statistical work, ~ 30 according to Nardiello et al. (2021). To enlarge the number of planets in OCs, both expanding the number of stars in clusters and identifying new OCs are feasible in the Gaia Era.

The Gaia DR2/EDR3 catalog (Gaia Collaboration et al. 2018; Lindegren et al. 2021) presents more than 1.3 billion stars with unprecedented high-precision astrometric and photometric data, greatly improving the reliability of stellar membership determination and characterization of a large sample of stellar groups including star clusters, association, and other comoving groups. The recent analysis of Gaia Data has



Original content from this work may be used under the terms of the [Creative Commons Attribution 4.0 licence](#). Any further distribution of this work must maintain attribution to the author(s) and the title of the work, journal citation and DOI.

greatly expanded our knowledge of stellar groups (e.g., Cantat-Gaudin et al. 2018; Kounkel & Covey 2019; Kerr et al. 2021). In previous knowledge, a star cluster is a set of stars that are gravitationally bound to one another (Portegies Zwart et al. 2010). However, the recent discovery of stars in diffuse regions reminds us that we need to extend the original definition of star clusters. Because these stars are in diffuse regions, i.e., not gravitationally bound, they are proven to have the same age as core cluster members through analyses of color–absolute magnitude diagrams (Kounkel & Covey 2019; Meingast & Alves 2019; Bouma et al. 2021). On top of that, these stars in diffuse regions also share a similar distribution with core cluster members in stellar rotation periods (Bouma et al. 2021) and chemical abundances (Arancibia-Silva et al. 2020; Hawkins et al. 2020). Therefore, these stars in diffuse regions are probably coeval. In this series of papers, we extend the definition of OCs to those stars in diffuse regions, i.e., comoving groups, diffuse streams, tidal tails, etc., not only the core cluster members. Thus, the number of stars in OCs can be extremely enlarged.

There are many previous works that identified new OCs in the Milky Way using different algorithms, e.g., Cantat-Gaudin et al. (2018) applied the UPMASK algorithm to select cluster members and provided an updated catalog of 1229 OCs; Cantat-Gaudin & Anders (2020) found 582 new cluster candidates located in the low galactic latitude area using an algorithm named Density-Based Spatial Clustering of Applications with Noise (DBSCAN), etc. Using Hierarchical Density-Based Spatial Clustering of Applications with Noise (HDBSCAN, McInnes et al. 2017), Kounkel & Covey (2019) systematically clustered Gaia DR2 data within 1 kpc and identified 1640 populations containing a total of 288,370 stars. In their recent work, Kounkel et al. (2020; hereafter K2020) extended the distance from 1 to 3 kpc and identified 8292 comoving groups consisting of 987,376 stars.

Utilizing the enlarged stellar population in clusters, the Understanding Planetary Formation and Evolution in Star Clusters (UPIc) project focuses on the planets in OCs, including association and other comoving groups. We are trying to find evidence of how planets form and evolve in cluster environments. Lots of works have shown that both dynamical (Spurzem et al. 2009; Liu et al. 2013; Cai et al. 2017; Hamers & Tremaine 2017; Rodet et al. 2021; Li et al. 2023) and radiation (Johnstone et al. 1998; Matsuyama et al. 2003; Dai et al. 2018; Winter et al. 2018) environments in clusters can influence the planet’s formation and evolution. As the initial work of UPIc, this paper collects the largest transiting planet sample in OCs and aims to analyze the correlation between the planetary radius and cluster ages, which is crucial for planet formation timescales. For example, (Szabó & Kiss 2011; Beugé & Nesvorný 2013; Mazej et al. 2016) discovered the hot Neptune desert in planetary mass–period and radius–period distribution. The boundaries of the desert can be explained by photoevaporation and high- e migration (Owen & Lai 2018). These two mechanisms have different timescales. Thus, the age of the planets can distinguish different mechanisms and help us understand the time evolution of planet radius.

This paper is arranged as follows. In Section 2, we describe methods, including data collection, age validation, and sample cut. In Section 3, we use these refined data to study the planet radius–age diagram and estimate the evolution of three

different planet populations. In Section 4, we discuss how the statistical results constrain the planet formation mechanisms, including high- e migration and photoevaporation. In Section 5, we discuss some additional influences and caveats. Last, we summarize our major conclusions in Section 6.

2. Catalog of Transiting Planet in OCs

2.1. Data Collection

There are many works that use Gaia data to identify new OCs. If we combine all the catalogs of star clusters, we can definitely get more OCs, and the stars in OCs. However, data selection criteria and clustering algorithms vary in different works, which will increase the inhomogeneity of the combined catalog. Therefore, to maximize the number of stars in OCs and make the sample as homogeneous as possible, we adopt the catalog from K2020, the largest catalog of stars with age estimations in comoving groups.

K2020 identified 8292 comoving groups within 3 kpc and galactic latitude $|b| < 30^\circ$ by applying the unsupervised machine learning algorithm HDBSCAN on Gaia DR2’s 5D data. We use the stellar catalog of K2020 to cross match with the host stars of confirmed transiting planets and planet candidates. In this section, we use planets/candidates from Kepler, K2, and TESS. Since we are concerned about the radius of planets, we do not consider planets detected via the radial velocity method. Sections 2.1.1–2.1.6 will briefly introduce how we select the planets and cut the planet sample to exclude some observation biases.

2.1.1. K2020 Cross Matching with Confirmed Exoplanets

The number of confirmed planets from the NASA exoplanets archive³ is 5347 up to now (2023 May, NASA Exoplanet Science Institute 2020a). After cross matching with K2020, we found 76 confirmed planets in clusters. To study the planet size–age distribution, we select 51 transiting planets with known planet radii.

The properties of planets and their host stars, e.g., planet radius, orbital periods, effective temperature, surface gravity, and stellar mass are adopted from the table of NASA exoplanets archive (NASA Exoplanet Science Institute 2020b). We adopt the age of the host stars from K2020 temporarily, which is completed. The adopted ages from K2020 will be validated via comparison in Section 2.2.

2.1.2. K2020 Cross Matching with KOIs

The number of KOIs from Kepler DR25 (Thompson et al. 2018) is 8445, including confirmed planets and candidates. After cross matching with K2020, we found 98 KOIs in clusters. Some of these KOIs may be False Positives, such as eclipsing binaries in the background of the targets or physically bound to them, which can mimic the photometric signal of a transiting planet. Then, we exclude the sources flagged as False Positive. There are 26 confirmed planets and 17 planet candidates in clusters for Kepler sources. Here, we use the Gaia–Kepler Stellar Properties Catalog (Berger et al. 2020) to update and obtain the accurate and precise properties of these 43 selected KOIs and their host stars. The age information is also adopted from K2020.

³ <https://exoplanetarchive.ipac.caltech.edu>

Table 1
Planets in Clusters

Name	R_p (R_{\oplus})	Period (days)	OName	Group	Gaia DR2	Age (Myr)	Validation	T_{eff} (K)	log g	Stmass (M_{\odot})	Flag
(1)	(2)	(3)	(4)	(5)	(6)	(7)	(8)	(9)	(10)	(11)	(12)
TOI 520.01	$1.49^{+0.66}_{-0.66}$	0.524	...	Group 95	5576476552334683520	$30.2^{+5.3}_{-4.5}$	NO	7450	4.34	1.66	TESS
TOI 626.01	$19.74^{+0.66}_{-0.66}$	4.40	...	Group 449	5617241426979996800	195^{+80}_{-57}	NO	8489	4.03	2.11	TESS
TOI 2453.01	$3.02^{+0.20}_{-0.20}$	4.44	Hyades	Group 1004	3295485490907597696	646^{+113}_{-96}	NO	3609	4.73	0.50	TESS
TOI 2519.01	$2.29^{+0.20}_{-0.20}$	6.96	Columba	Group 208	2924619634745251712	263^{+109}_{-77}	NO	4742	4.57	0.76	TESS
TOI 2640.01	$7.39^{+0.50}_{-0.50}$	0.911	IC 2602	Group 92	5404579488593432576	45^{+14}_{-11}	NO	2999	4.95	0.25	TESS
TOI 2646.01	8.10	0.313	NGC 2516	Group 613	5288535107223500928	145^{+37}_{-30}	NO	5202	4.53	0.88	TESS
TOI 2822.01	$11.53^{+0.72}_{-0.72}$	2.88	...	Group 5076	5597777288033556480	537^{+94}_{-80}	NO	6086	4.04	1.14	TESS
TOI 3077.01	$13.67^{+0.72}_{-0.72}$	6.36	...	Group 3176	5307513536932390272	186^{+130}_{-71}	NO	7689	4.06	1.80	TESS
TOI 3335.01	$11.60^{+0.70}_{-0.70}$	3.61	...	Group 550	5903623451060661504	214^{+75}_{-55}	NO	6071	4.04	1.13	TESS
TOI 1097.02	$12.7^{+1.0}_{-1.0}$	2.27	...	Group 1502	6637496339607744768	3020^{+447}_{-390}	NO	5568	3.89	0.98	TESS
...

Note. Due to the space limitation, we only show the first 10 rows of the table. Here, “OName” shows the name of the parental cluster, “Group” shows the corresponding group number in [K2020](#), “Flag” shows the name of the mission that detects the planets, and “Validation” shows whether this planet/candidate has the convincing age estimation (i.e., “YES,” “NO,” and “Excluded”).

(This table is available in its entirety in machine-readable form.)

2.1.3. [K2020](#) Cross Matching with *K2*

For *K2* sources we use the catalog of *K2*, including both confirmed planets and candidates from the NASA exoplanet archive, to cross match with [K2020](#). We get only 25 matching sources. After excluding nine candidates flagged as “FALSE POSITIVE,” we obtained nine confirmed planets and seven planet candidates with planet radius measurements. The properties of planets and planets’ host stars are taken from the NASA exoplanet archive. The age information is taken from [K2020](#).

2.1.4. [K2020](#) Cross Matching with *TOIs*

Up to 2023 May, there are 6586 *TOIs* detected by TESS. After cross matching with [K2020](#), there are 116 *TOIs* left. There are many False Positives in *TOIs* (Gan et al. 2023). Thus, we select the *TOIs* carefully. First, we exclude some sources flagged as “FA,” “APC,” and “FP,” which means false alarm, ambiguous planet candidate, and false positive, respectively. After exclusion, 68 *TOIs* are left. Besides, based on publicly available observational notes on ExoFOP,⁴ we also remove some *TOIs* with comments like “centroid offset,⁵” “V-shaped,” “Likely eclipsing binary (EB),” and “odd–even.” For example, the comment of *TOI* 1376.01 is “centroid offset on TIC 190743999 in spoc-s56.” After removing these *TOIs*, we finally select 42 *TOIs*, i.e., 12 confirmed planets and 30 candidates. The properties of these 42 selected *TOIs* and their host stars are taken from the table of *TOIs*. The age information is taken from [K2020](#).

2.1.5. Other Sources

[K2020](#) focuses on the stars with galactic latitude $|b| < 30^\circ$. Actually, there are many other clusters out of such range, and so do the planets in clusters. We add the planets and planet candidates in the PATHOS project to include more planets at

higher galactic latitudes. Table 6 of PATHOS-IV (Nardiello et al. 2021) provides 33 confirmed planets in clusters. Although 11 confirmed planets are repeated selected planets in Section 2.1.1, 14 of them are with $|b| > 30^\circ$, and eight of them are uncross matched with [K2020](#). Additionally, the PATHOS project has found 90 planet candidates in clusters, which are not included in *TOI* completely. After cross matching with [K2020](#), we get the age information of 40 planet candidates with $|b| < 30^\circ$. Here, we do not include the candidates of the PATHOS project with $|b| > 30^\circ$ because they do not have the age measurements. Nardiello et al. (2021) provide false positive probabilities for the PATHOS candidates. We removed eight sources with high false positive probabilities. Most of them are likely eclipsing binaries. Thus, we add 32 PATHOS candidates. The stellar properties are taken from the TESS Input Catalog v8.0 (TIC-8, Stassun et al. 2019), e.g., stellar mass, stellar effective temperature, and surface gravity.

2.1.6. The Catalog of Transiting Planets in Star Clusters

After the cross matching, we check the catalog of transiting planets in clusters and exclude the repeated planets. Finally, there are 73 confirmed planets and 84 planet candidates in 86 clusters. Table 1 shows all these planets in 133 planetary systems. Planets detected by different missions are flagged as “Kepler,” “*K2*,” “TESS,” and “other.” Here, “other” means sources detected by other facilities, e.g., CoRoT (Léger et al. 2009) and ground-based telescopes.

This is the largest catalog of the planets and planet candidates in star clusters. Due to space constraints, we only list 10 sources in Table 1. The whole table can be downloaded in a machine-readable format.

2.2. Age Validation

Since we focus on the age–size distribution of planets in clusters, the accuracy and precision of age measurements are essential. In this section, we will compare the age measurement of stars from He et al. (2022; hereafter He2022), [K2020](#), and the table of the NASA exoplanet archive to illustrate whether

⁴ <https://exofop.ipac.caltech.edu/tess/>

⁵ The light from nearby eclipsing binaries within $1''$ may pollute the aperture and cause transit-like signals on the target light curve, especially in a crowded field like OCs.

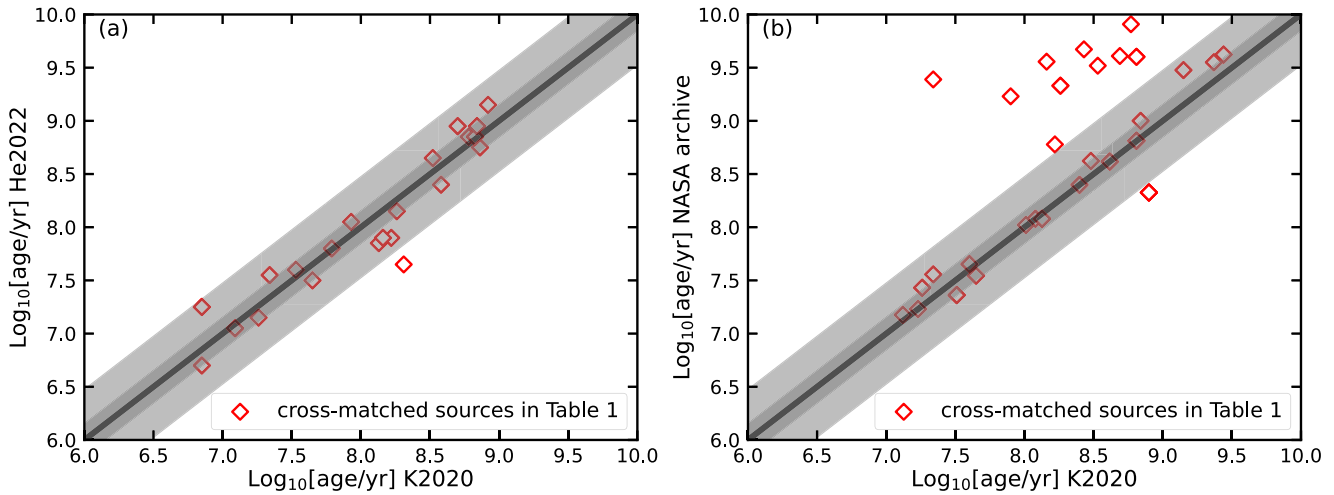


Figure 1. The comparison of age estimation from different catalogs. Panel (a) uses data from the cross matching catalog of **K2020** and **He2022**. Panel (b) uses data from **K2020** and the NASA exoplanet archive. Gray shadows are 1σ and 3σ areas considering the average uncertainty of age estimation of comoving groups within 1 kpc in **K2020**. A black solid diagonal line is plotted for reference.

the age estimation in **K2020** is robust. Kounkel et al. (2020) adopted a neural network called Auriga to robustly estimate the ages of the individual groups they identified. The uncertainty of $\log(\text{Age})$ of comoving groups within 1 kpc in **K2020** is similar to Kounkel & Covey (2019), i.e., ~ 0.15 dex. In **He2022**, they used the isochrone fitting to derive the ages of 886 nearby clusters and candidates within 1.2 kpc.

Although Kounkel et al. (2020) discuss the contamination and demonstrate that the vast majority of the ages are well consistent with the results of isochrone fitting, the age estimation in **K2020** may still have some systematic biases compared to **He2022**. On top of that, the difference in identifying clusters may also influence the final age estimation. **K2020** used unsupervised machine learning HDBSCAN to identify clusters, while **He2022** used DBSCAN. HDBSCAN has a better performance on the data with different density structures than DBSCAN, i.e., it prefers to reveal more fine structures. Therefore, both the age estimation and the cluster membership identification will lead to systematic biases.

Then, we cross matched the catalog of **K2020** and **He2022** to present whether the bias of age estimation in **K2020** is non-negligible compared to other age sources. In panel (a) of Figure 1, red hollow dots are the 36 planets/candidates in 22 clusters that both have the age estimation in **K2020** and **He2022**. Only one planet candidate has a large difference in age estimation out of the 3σ limit, i.e., the PATHOS 64 in King-6. Therefore, we assume that the majority of the age estimation in **K2020** is relatively robust. To validate the ages of this cluster, we refer to the ages from other previous works. In **K2020**, the estimation of the age of King-6 is 204_{-63}^{+91} Myr, which is consistent with the previous result of Ann et al. (2002; 250 ± 50 Myr), while in **He2022**, the age of King-6 is 44 Myr without uncertainty. Thus, we adopt 204_{-63}^{+91} Myr as the final age of King-6.

Additionally, we also compare the age of the **K2020** and the NASA exoplanet archives. In panel (b) of Figure 1, there are 29 planet host stars (44 planets) in our catalog with both ages from **K2020** and NASA exoplanet archives. A total of 11 host stars are out of the 3σ limit in the age measurement, i.e., CoRoT-22, HATS-47, HD 110113, KELT-20, Kepler-1062, Kepler-1118, Kepler-1502, Kepler-411, Kepler-968, TOI-1937

A, and TOI-4145 A. All the ages of these planets' host stars from NASA exoplanet archives are much larger than the ages from **K2020**. Exempli gratia, the age of CoRoT-22 is 3.3 ± 2.0 Gyr in Moutou et al. (2014), while in **K2020** is 339 ± 100 Myr; the age of HATS-47 in Hardegree-Ullman et al. (2020) is $8.10_{-4.30}^{+2.90}$ Gyr, while in **K2020** is 589_{-171}^{+243} Myr; the age HD 110113 (Osborn et al. 2021) is 4.0 ± 0.5 Gyr, while in **K2020** is 645_{-178}^{+245} Myr.

The individual age estimation of these stars depends on the models and methods, which are inhomogeneous in the NASA exoplanet archive. Strictly, we use different ways to validate the ages of the 11 host stars.

First, some stars may have several (≥ 3) age measurements, which we can evaluate through majority voting. For instance, the age estimation of KELT-20 is ≤ 0.6 Gyr, according to Lund et al. (2017). However, according to Talens et al. (2018), KELT-20 is 200_{-50}^{+100} Myr, which is consistent with **K2020**'s result, i.e., 166_{-43}^{+58} Myr. The age estimation of Kepler-1118 from Morton et al. (2016; 4.07 Gyr) is nearly 10 times of that in **K2020** (490_{-118}^{+155} Myr). We strengthen that Morton et al. (2016) set the age prior to 1–15 Gyr, which means the stellar age in their catalog is artificially larger than 1 Gyr. As the host cluster of Kepler-1118, NGC 6866 has an age of 705 ± 140 Myr from Janes et al. (2014). Therefore, we adopt the age in **K2020** for KELT-20 and Kepler-1118.

Second, if stars do not have independent and consistent age measurements, we estimate the age via the gyrochronological relation. Kepler-411 is a special case where three age measurements are significantly different. Sun et al. (2019) use gyrochronological relation (Barnes 2007) and estimate an age of 212 ± 31 Myr, **K2020** estimates an age of 794_{-219}^{+302} Myr, and Morton et al. (2016) estimate an age of $2.69_{-1.10}^{+2.67}$ Gyr. To validate the age of Kepler-411, we adopt the new gyrochronological relation, which includes the empirical mass dependence of the rotational coupling timescale developed by Spada & Lanzafame (2020). The stellar rotation period of Kepler-411, 10.4 days, is taken from McQuillan et al. (2013). Then, we estimate an age of 770 Myr for the Kepler-411 system, which is consistent with the age estimation in **K2020**. Thus, we adopt 794_{-219}^{+302} Myr as the age of Kepler-411.

Table 2
Sample Cut of Planets/Candidates in Clusters

Criterion	Planets	Planet Candidates
The whole number	73	84
Age validation	63	84
$R_p < 2.5 R_J$	62	62
$RUWE < 1.4$	62	53
$\sigma_{R_p}/R_p < 0.5$	58	50
$P < 20$ days	37	44
$R_p > 2R_\oplus$	30	36

The same with Kepler-411, we use the rotating period and stellar mass, and obtain the ages of HATS-47, HD 110113, Kepler-1062, and Kepler-968, through the new gyrochronological relation, i.e., <0.1 Gyr, ~ 3 Gyr, ~ 1.3 Gyr, and ~ 0.7 Gyr, respectively. These age estimations are significantly different from K2020 (i.e., 589_{-171}^{+243} Myr, 645_{-178}^{+245} Myr, 21_{-4}^{+4} Myr, and 181_{-41}^{+52} Myr, respectively). We speculate that HATS-47, HD 110113, Kepler-1062, and Kepler-968 may be the contaminating stars in star cluster identification. They may be field stars having similar kinematic properties compared to the comoving stellar groups in their proximity, coincidentally. Therefore, we exclude these three potential contaminating sources in cluster identification. We also removed HATS-47 because it does not have a convincing age measurement.

Third, for CoRoT-22, Kepler-1502, TOI-1937 A b, and TOI-4145 A b, which have inconsistent age measurements and lack of stellar rotation measurements, we can hardly validate their age. Additionally, Yee et al. (2023) suspect that TOI-1937 A and TOI-4145 A may be the field star because of the poorly constrained cluster membership identification. Therefore, we directly exclude these four systems.

To sum up, we validate the age measurement of 70 planets/candidates in star clusters, obtain more convinced ages of three host stars via either literature or the new gyrochronological relation, and exclude eight planetary systems without convincing age estimations. If we assume those eight host stars are field stars, the contamination rate of our catalog is about 6%, which is consistent with that in Kounkel & Covey (2019), i.e., 5%–10%.

2.3. Sample Cut

In Section 2.2, we obtain 63 planets and 84 planet candidates in star clusters with relatively robust age estimation. We aim to obtain the planet radius evolution, i.e., planet radius–age distribution. The accuracy of planet radius and age measurements will significantly influence our results. Therefore, we need to do the sample cut to minimize the influence of observational biases.

Here, we list the steps of the sample cut in Table 2. Without the mass measurement, we can hardly determine whether the planet candidates are planets or brown dwarfs. Planet candidates with large radii are unlikely planets. Thus, we exclude 23 planets/candidates with $R_p > 2.5 R_J$ (the same criteria described in Nardiello et al. 2021). Brown dwarfs with larger masses can induce the motion of the photon center. Berger et al. (2020) suggest that stars with high renormalized unit weight error ($RUWE > 1.4$) are likely to be binaries. Although a few confirmed astrometric planets from Gaia (Holl et al. 2023) have ($RUWE > 1.4$), most stars with confirmed

planets are below this threshold. Thus, we adopt the criteria $RUWE < 1.4$ to exclude nine planet candidates in potential binary systems. Since planets with poor radius measurements may contaminate the results, we exclude seven samples with relative radius errors larger than 50%. Due to the precision of TESS and the stellar noise of young stars, small planets detected by TESS and planets around young stars are less complete. Thus, we need to constrain the lower limits of the planet radius to exclude the bias of completeness. As shown in Appendix A, planets with radius $R_p > 2 R_\oplus$ and period $P < 20$ days could be detected (signal-to-noise ratio; $S/N > 7.1$) via both Kepler and TESS. Thus, we cut the sample via $R_p > 2 R_\oplus$ and $P < 20$ days.

After the sample cut, there are 66 planets/candidates left. In Section 3, we mainly use the sample to do the analysis.

3. Planet Radius–Age Distribution

3.1. Planet Radius–Age Diagram

Figure 2 shows the planetary size–age distribution of 37 planets and 44 planet candidates in star clusters (15 planets/planet candidates with $R_p < 2 R_\oplus$ and 66 planets/planet candidates with $2 R_\oplus < R_p < 2.5 R_J$).

Here, we classify planets into three groups by size for the sake of simplicity:

1. Sub-Neptunes, i.e., planets of $2 R_\oplus < R_p < 4 R_\oplus$,
2. Sub-Jupiters, i.e., planets of $4 R_\oplus < R_p < 8 R_\oplus$,
3. Jovian planets, i.e., planets of $8 R_\oplus < R_p < 2.5 R_J$.

There are only five Jovian planets younger than 100 Myr, while dozens beyond 100 Myr. So, it seems that there is a gap in the planet radius–age diagram for the Jovian planets younger than 100 Myr. Additionally, there may be another gap for sub-Jupiters with ages between 50 and 200 Myr. Before 50 Myr, there are several sub-Jupiters, while between 50 and 200 Myr, the number of sub-Jupiters declines to nearly none. On top of that, there are nearly no sub-Neptunes between 50 and 100 Myr.

Therefore, it seems that all of the planets disappear between 50 and 100 Myr. However, due to the small number of planets/candidates (i.e., the large statistical error), whether the gap is real cannot be easily demonstrated. In order to avoid observational bias, in Section 3.2, we will take into the age error and the radius error of the planets to obtain the time-dependent relation for the proportion (instead of the number) of different-sized planets in star clusters.

3.2. The Evolution of Planet Radius

In this section, we will show our main results of the time-dependent relation of different-sized planets in Section 3.2.1 and some influence of contamination in Section 3.2.2.

3.2.1. Main Results

To investigate the time-dependent relation of different-sized planets in star clusters. We defined the proportions of planets with different sizes and ages. To determine the proportions and the uncertainties, we randomize the ages and radii of all the planets 100,000 times, assuming the Gaussian distribution. Then, we can obtain the proportions of each time, denoted as f_i ,

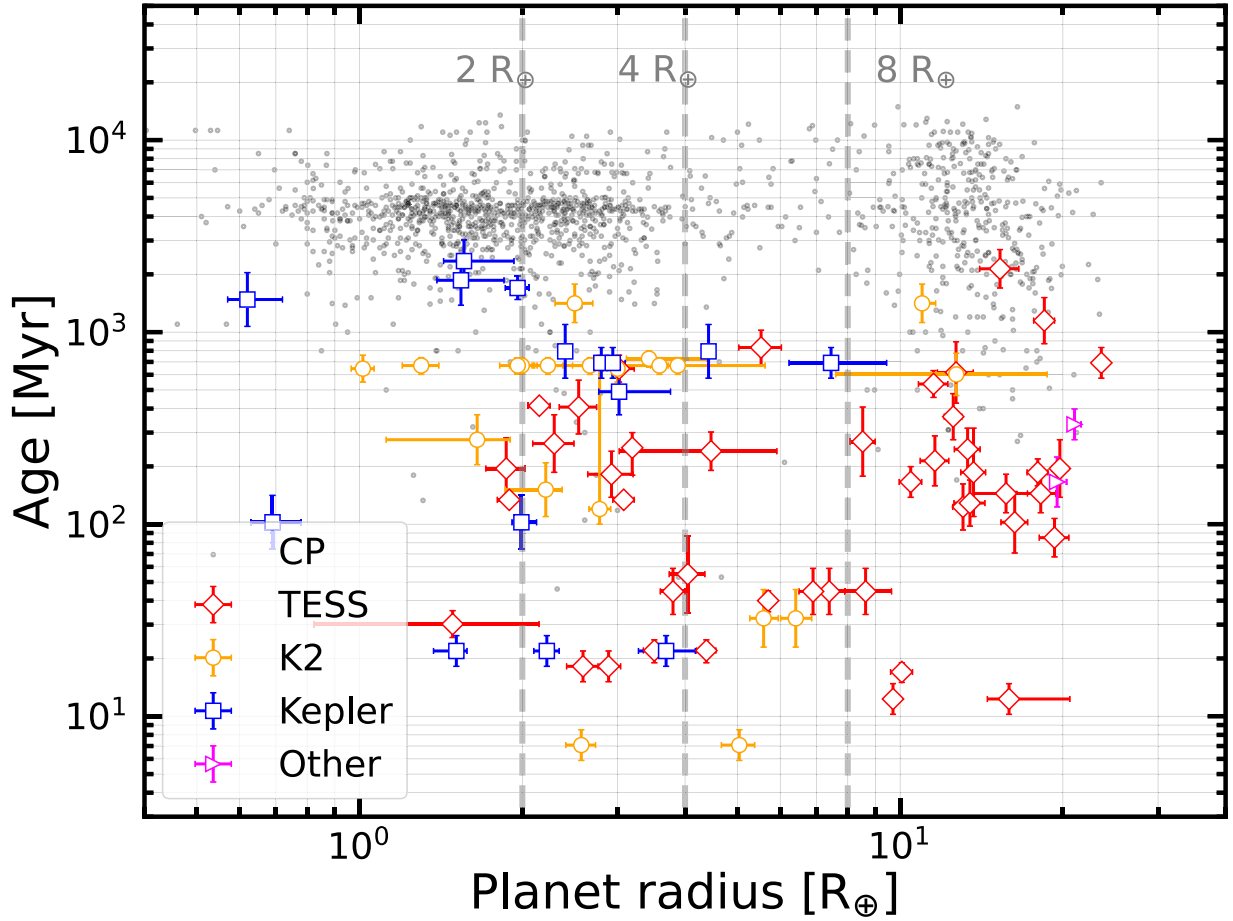


Figure 2. The planetary radius–age distribution of 37 planets and 44 planet candidates in star clusters (Table 2). Different colors show the planets in clusters detected by different missions. Red, yellow, blue, and purple symbols are planets/candidates detected by different missions, i.e., Kepler, K2, TESS, and other ground-based telescopes, respectively. The gray dots are confirmed transiting planets whose host stars have age measurements.

via the formula:

$$f_i = \frac{N_i}{N_{\text{SubN}} + N_{\text{SubJ}} + N_J}, \quad (1)$$

where N_i is the number of planets in star clusters with different sizes, i.e., N_{SubN} , N_{SubJ} , or N_J corresponding to sub-Neptunes, sub-Jupiters, and Jovian planets in Section 3.1, respectively. After calculating 100,000 times, we obtain the distribution of f_i and adopt the lower limits, median values, and the upper limit, according to the 16, 50, and 84 percentiles of f_i , respectively. The results are shown in Figure 3. Note the age is cut by ≤ 1 Gyr because most of the selected planets/candidates in star clusters are younger than 1 Gyr (Figure 2). Panels (a) and (b) are different in the number of age bins, i.e., four and eight age bins between 10 and 1000 Myr under the log scale, respectively. Both two panels show that the proportion of Jovian planets (red diamonds, f_J) increases before 100 Myr and then declines after 200 Myr, i.e., a peak occurs between 100 and 200 Myr. The proportion of sub-Jupiters (blue squares, f_{SubJ}) declines around 100 Myr. The proportion of sub-Neptunes (gray circles, f_{SubN}) shows a clear increase after 100 Myr. Here, we also consider the Poisson error because of the small number of planets in each bin, which has similar features to Figure 3 (see Figure B1 in Appendix B).

To extend the evolution of planets/candidates older than 1 Gyr, we calculate the proportion of planets both in star clusters and around field stars with different sizes. Here, we add ~ 871 confirmed planets with age measurements from the NASA Exoplanet Archive. These confirmed planets share the same cut with planets/candidates in star clusters, i.e., $2 R_{\oplus} < R_p < 2.5 R_J$, and $P < 20$ days. Using the same estimating procedures as those in Figure 3, we obtained the proportion varying with age, as shown in Figure 4.

In panels (a) and (b) of Figure 4, the proportion of Jovian planets (red diamonds, f_J), sub-Jupiters (blue squares, f_{SubJ}), and sub-Neptunes (gray circles, f_{SubN}) show a similar time-dependent relation within 1 Gyr to that in Figure 3. That is, f_J reaches a maximum between 100 and 200 Myr, f_{SubJ} rapidly declines around 100 Myr, and f_{SubN} increases after 100 Myr. Because Figure 4 has a longer time span than Figure 3, there are more substructures in Figure 4. For example, all of the panels in Figure 4 show a tiny bump of f_J around 2 Gyr, which is anticorrelated with f_{SubN} , i.e., a small dip of f_{SubN} around 2 Gyr. These two timescales, i.e., 100 Myr and 2 Gyr (gray shadow regions), may correspond to different planet formation environments (see discussion in Section 4.2). Because the majority of planets younger than 300 Myr are in star clusters, while most of the planets older than 1 Gyr are around field stars.

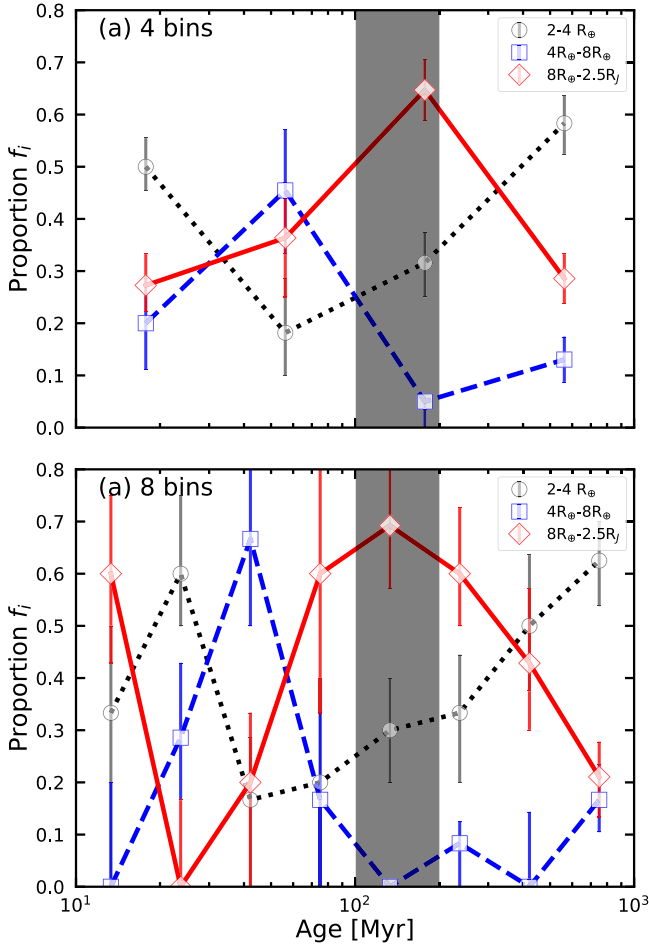


Figure 3. The time-dependent relation of the proportions of planets (in star clusters) of different sizes. Different colors show planets of different sizes. Panels (a) and (b) are different in the number of age bins, i.e., four age bins between 10 and 1000 Myr under log scale in panel (a), and eight age bins in panel (b).

To illustrate that our results are robust, we should exclude the influence of some other stellar parameters. For example, some planet host stars are very hot, i.e., $T_{\text{eff}} > 7500$ K, especially for the candidates detected by TESS. For main-sequence stars, hotter stars usually have larger stellar radii than cooler ones. Therefore, the transit method tends to find larger planet candidates around hotter stars. In panel (c), we add another criterion for planets/candidates in star clusters and around field stars, i.e., $T_{\text{eff}} < 7500$ K. Although the proportion of Jovian planets f_J around 200 Myr is smaller than that in panel (b) because of the additional sample cut, f_J still continuously increases between 100 and 400 Myr, i.e., the peak moves backward to around 400 Myr. The proportion of f_{SubJ} rapidly decreases around 100 Myr, then remains at ~ 0.1 after 100 Myr, similar to that in panel (b). f_{SubN} does not show an obvious increase/decrease after 100 Myr.

The widely used definition of HJs is Jupiter-sized planets within 10 days (Dawson & Johnson 2018). Here, in panel (d), as a comparison, we also show the results of the conventional hot planets within 10 days. For Jovian planets and sub-Jupiters, panel (d) shows similar results to panel (b). Therefore, in the following, we call the Jovian planets within 20 days as HJs for simplicity (if without additional annotation). For sub-Neptunes, the increasing tendency after 100 Myr is ambiguous.

In panel (e), we show the results of the time-dependent relation of planet radius for planets within 200 days. Because including some warm planets, the increment of f_J around 100 Myr in panel (e) becomes less than that in panel (b). As the majority of the warm planets are sub-Neptunes, f_{SubN} in panel (e) is systematically higher than that in panel (b) after 100 Myr. In turn, the f_J in panel (e) is systematically lower than that in panel (b) after 100 Myr. The time-dependent relation of f_{SubJ} in panel (e) is similar to other panels.

In Figure 4, we cannot find an obvious increase trend in the proportion of sub-Neptunes within 1 Gyr, as shown in Figure 3. Because it seems sensitive to the parameter cut.

3.2.2. Influence of Some Contamination

To test the robustness of our statistical results, we also check some other influences, e.g., the criteria of planet radius cut and the potential false positives in planet candidates.

First, we will discuss the criteria of planet radius cut. Young giant planets with an expanded radius may still go through the contraction, which means the exclusion of young candidates with $R_p > 2.5R_J$ may underestimate the f_J . We checked the 23 candidates with $R_p > 2.5R_J$ in Section 2.3 and found that most of them are around 100 Myr. If we consider these candidates, it will enhance the peak of f_J between 100 and 200 Myr.

Second, to avoid the influence of potential false positives, we only use confirmed planets to drive the time-dependent relation of planet radius. The results are shown in Figure C1 in Appendix C, which is similar to that of containing planet candidates. Therefore, our statistical results are robust.

To summarize Section 3.2, we obtain the time-dependent relation of planet radius for planets/candidates in star clusters and around both cluster members and field stars, i.e.,

1. The proportion of Jovian planets f_J increases around 100 Myr and reaches a maximum between 100 and 200 Myr, which is mainly attributed to the HJs in star clusters. The tiny bump of f_J around 2 Gyr is attributed to the HJs around field stars.
2. The proportion of sub-Jupiters f_{SubJ} declines rapidly around 100 Myr, then remains at a low value. The decl. of f_{SubJ} is mainly attributed to the hot sub-Jupiters in star clusters.

4. Constraints of Hot Giant Planets Formation Timescale

Based on the statistical results above, we try to explain or constrain the timescales of hot giant planets' formation mechanisms in star clusters. Here, the hot giant planets mean HJs and hot sub-Jupiters (or hot Neptunes).

There are several formation scenarios of HJ, i.e., in situ formation when disk mass is large, or ex situ formation then undergoing disk migration or high- e migration. The timescales of the first two HJ formation scenarios are mainly limited by the lifetime of the gas disk, which is typically ~ 10 Myr. Therefore, if the in situ formation and disk migration are the dominant channels of HJ formation, the number of HJs will not significantly change after 10 Myr. However, Figures 3 and 4 show that the proportion of HJs (f_J) has an obvious increment around ~ 100 Myr, which is probably attributed to the high- e migration.

Note that we do not exclude the possibility of HJs forming through the in situ formation and disk migration. However,

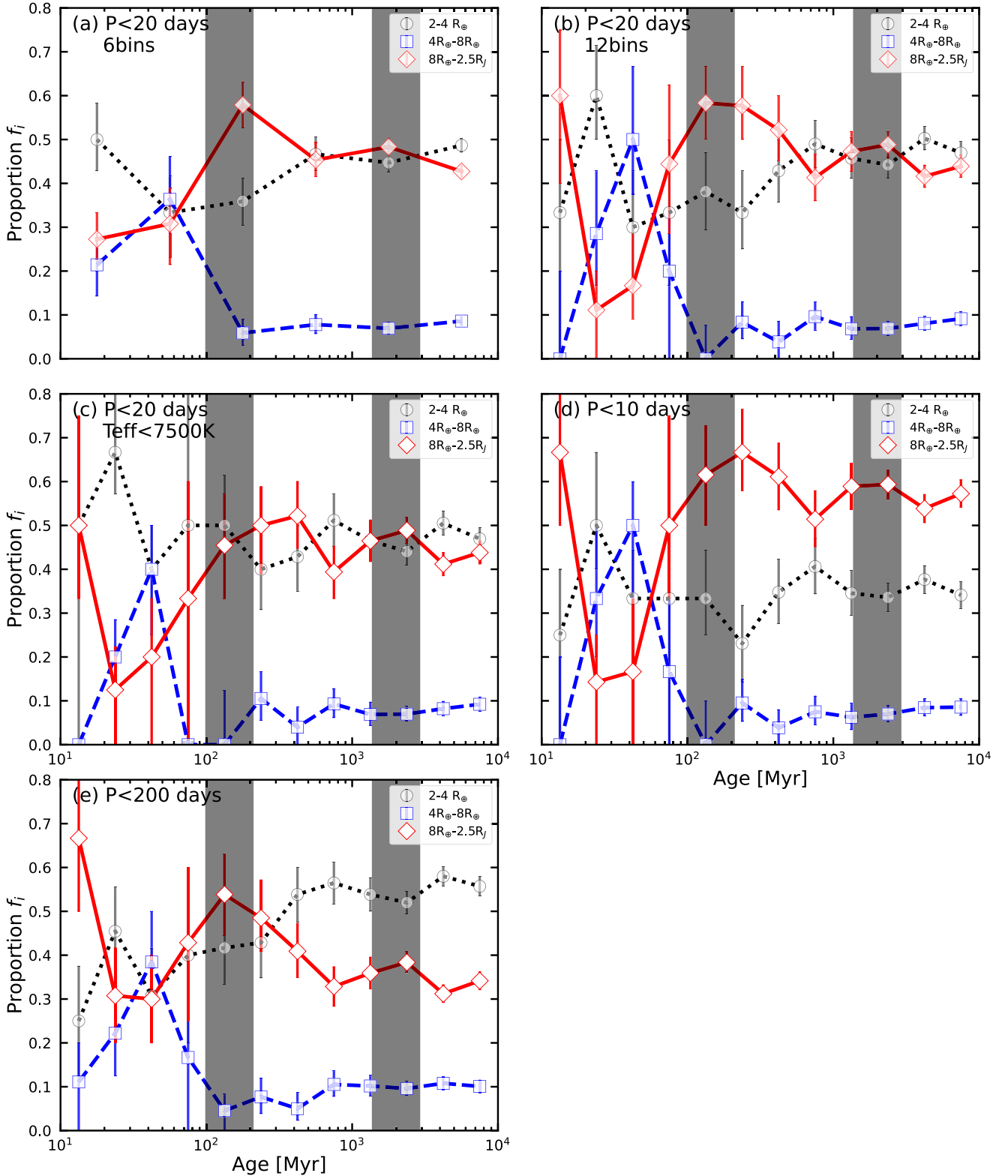


Figure 4. The time-dependent relation of the proportions of planets (both in star clusters and probably around field stars) of different sizes. Different colors show planets of different sizes. Panels (a) and (b) are different in the number of age bins, i.e., six age bins between 10 and 10,000 Myr under log scale in panel (a) and 12 age bins in panel (b). We add a cut of effective temperature in panel (c) and an additional period cut in panel (d), i.e., $P < 10$ days. For panel (e), we show the result for planets with $P < 200$ days as a comparison. Two shadow regions around 100 Myr and 2 Gyr are overlotted to emphasize two typical timescales.

with a lack of clusters younger than 10 Myr, we can hardly constrain the in situ formation mechanism and the fraction of such planets.

In the following discussion, we mainly focus on the increment of f_j and the rapid decl. of f_{SubJ} around 100 Myr in star clusters. More specifically, in Section 4.1, we estimate the

timescales of flyby-induced high- e migrations in star clusters using typical parameters. In Section 4.2, we try to explain the tiny bump of HJs, as well as the small dip of sub-Neptune. The hot Neptune desert is also discussed in Section 4.3. Some preliminary results of warm Jupiters are shown in Section 4.4 to support flyby-induced high- e migrations in star clusters.

4.1. Flyby-induced High- e Migration in Open Clusters within 200 Myr

Recently, several observation works have shown environments in clusters can influence planet formation and evolution (Winter et al. 2020; Dai et al. 2021). In star clusters, especially dense clusters, close stellar flybys may occur frequently. A series of theoretical works have shown that the HJ formation can be triggered by stellar flybys in star clusters (Li et al. 2020, 2023; Wang et al. 2020, 2022; Rodet et al. 2021). Similar to previous works, we consider hierarchical planet systems with both Jovian planets and an outer companion (e.g., a cold giant planet, substellar, or stellar companion). The high- e migrations of the Jovian planet induced by flybys can be described as follows. During a close flyby event, a flyby star exchanges the angular momentum with the outer companion and excites its eccentricity and inclinations. Consequently, the eccentricities of the Jovian planets will be highly excited through the von Zeipel–Lidov–Kozai mechanism (ZKL, von Zeipel 1910; Kozai 1962; Lidov 1962). Finally, tidal circularization leads to the inward migration of the Jovian planet.

There are three factors determining the formation timescale of HJs under flyby-induced high- e migration in star clusters, i.e., the timescale of the close flyby (τ_{flyby}), the ZKL mechanism (τ_{ZKL}), and the tidal circularization (τ_{tidal}). Roquette et al. (2021) demonstrate that an effective stellar flyby means flyby with small periastron q , which can trigger the ZKL oscillation successfully and subsequently excite the high eccentricity of the inner Jovian planet. Here, we combine Equations (17), (18), and (19) in Roquette et al. (2021) to get an estimation of τ_{flyby} , the timescale of an effective flyby, i.e.,

$$\tau_{\text{flyby}} = \left(\frac{10^3 \text{ pc}^{-3}}{n_*} \right) \left(\frac{2 M_\odot}{M_{\text{tot}}} \right) \left(\frac{50 \text{ au}}{a_{\text{out}}} \right) \left(\frac{\sigma_*}{1 \text{ km s}^{-1}} \right) \text{ Gyr}, \quad (2)$$

where n_* is stellar density in clusters, M_{tot} is the total mass of the hierarchical three-body system, a_{out} is the semimajor axis of the outer companion, and σ_* is the velocity dispersion of star clusters. Here, we assume a solar Jupiter system plus a solar-like companion, i.e., $M_{\text{tot}} \sim 2 M_\odot$. Other parameter settings are as follows: $n_* = 10^4 \text{ stars pc}^{-3}$, $a_{\text{out}} = 50 \text{ au}$, and $\sigma_* = 1 \text{ km s}^{-1}$. The setting of $\sigma_* = 1 \text{ km s}^{-1}$ and $a_{\text{out}} = 50 \text{ au}$ are the same as Rodet et al. (2021).

In the following, we describe the reason for the parameter setting of stellar density. According to the hierarchical star formation scenario (Kruijssen 2012) and recent Gaia DR2 observation (Anders et al. 2021), only a small number of stars (<30%) have originated from the bound clusters. That is, most stars have originated from relatively low-mass stellar groups. Unlike bound OCs, which probably span over several hundreds of million years, low-mass stellar groups in the solar neighborhood with filamentary substructures are usually younger than 100 Myr (Pang et al. 2022). They may disperse and become associations, e.g., some of the associations might be originally linked to OCs (Gagné et al. 2021). Some earlier works (e.g., Adams 2010; Malmberg et al. 2011;

Craig & Krumholz 2013) assume that high stellar density can only exist in the high-mass clusters. However, recent work (Pfalzner & Govind 2021) revealed that low-mass clusters share a similar flyby frequency with high-mass clusters, at least in the early stage of cluster evolution. Thus, it is reasonable to assume the typical density of star clusters in their early stage as $10^4 \text{ stars pc}^{-3}$. Then, the timescale of an effective flyby τ_{flyby} is about 100 Myr.

The ZKL timescale (τ_{ZKL}) can be estimated as Wang et al. (2022):

$$\tau_{\text{ZKL}} = P_{\text{in}} \left(\frac{M_{\text{tot,in}}}{M_{\text{out}}} \right) \left(\frac{a_{\text{out}}}{a_{\text{in}}} \right)^3 (1 - e_{\text{out}}^2)^{3/2} \quad (3)$$

where P_{in} is the orbital period of the inner Jovian planet, $M_{\text{tot,in}}$ is the total mass of the Sun–Jupiter system, M_{out} is the mass of outer companion, and the e_{out} is the eccentricity of the outer companion. If we assume that the inner Jupiter forms outside the water ice line around 2.7 au, i.e., $a_{\text{in}} \sim 2.7 \text{ au}$ and $P_{\text{in}} \sim 4.4 \text{ yr}$, the typical ZKL timescale τ_{ZKL} is $\sim 0.3 \text{ Myr}$, which is much shorter than τ_{flyby} .

According to Figure 2 in Rodet et al. (2021), an effective flyby can successfully lead to the high-eccentric orbit of the inner planet, typically larger than 0.99. For HJs in star clusters, the median value of the orbital period is around 3 days, which corresponds to 0.04 au around a Solar-like star. If we set the final semimajor axis ($a_f = 2q_{\text{in}}$, Owen & Lai 2018) after tidal circularization of a Jovian planet as 0.04 au, the periastron of the inner planet q_{in} is about 0.02 au. According to Figure 1 or Equation (5) in Wang et al. (2022), the typical tidal dissipation timescale of such a system is $\lesssim 100 \text{ Myr}$. Therefore, the typical formation timescale of HJs (τ_{HJC}) through flyby-induced high- e migration is $\lesssim 200 \text{ Myr}$ under our parameter settings. Due to the uncertainty of the mass of outer companions, τ_{HJC} may move backward to several hundreds of Myr. In some cases, if we take into account chaotic or diffusive tides (e.g., Mardling 1995a, 1995b), planets may experience quicker tidal circularization than that under the scenario of equilibrium tides. That is, the high-eccentricity migration process can be sped up in its early stages at high eccentricities, Vick & Lai (2018). To sum up, HJs can form through flyby-induced high- e migration in OCs within 200 Myr.

Dawson & Johnson (2018) provide that the occurrence rate of HJs is 0.5%–1%, which is 10 times of estimation by Roquette et al. (2021). Interestingly, if we adopt the new stellar density value in Pfalzner & Govind (2021; i.e., $n_* = 10^4 \text{ pc}^{-3}$), the observed HJs can be successfully explained by flyby-induced high-eccentricity migration in star clusters. This may indicate that the flyby-induced high- e migration is the dominant formation scenario of HJ in star clusters. One intriguing system may be consistent with our scenario, i.e., Pr0211 b&c. Pr0211, a member of Praesepe ($\sim 700 \text{ Myr}$), has two giant planets surrounding it. One is a HJ within 3 days, i.e., Pr0211 b with near-circular orbit, and the other, Pr0211 c, is a cold Jupiter beyond 3500 days with a very eccentric orbit ($e > 0.6$, Malavolta et al. 2016). Pfalzner et al. (2018) demonstrate that a stellar flyby scenario could shape the Pr0211 system successfully.

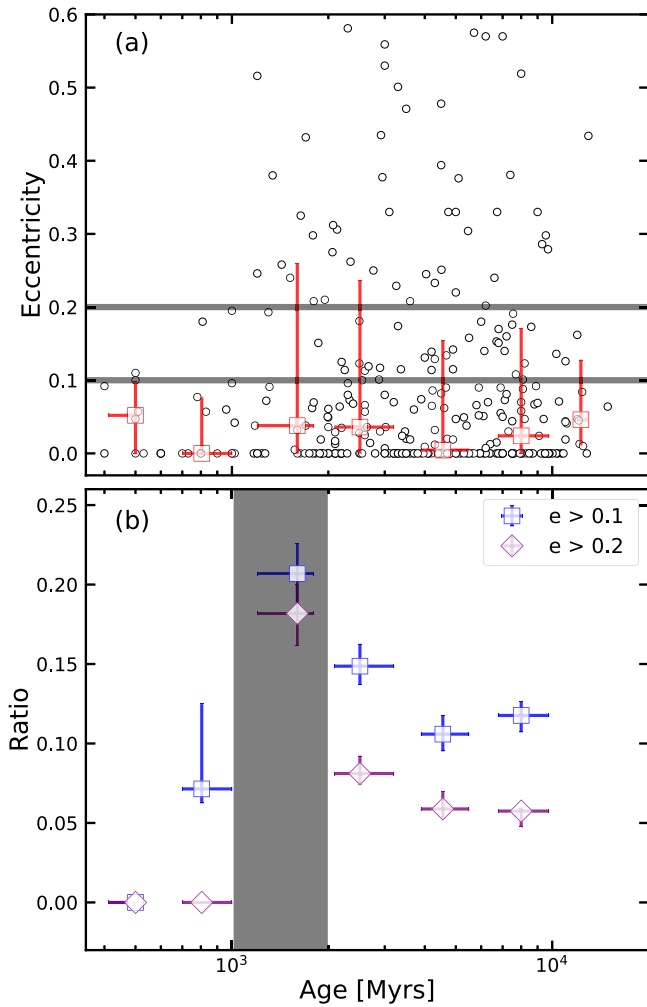


Figure 5. The eccentricity–age relation of HJs. We select 336 known HJs ($P < 20$ days, $\sigma_{R_p}/R_p < 0.5$) with age and eccentricity measurements. Panel (a) shows the entire sample in the eccentricity–age diagram. Panel (b) represents the ratio of high-eccentricity HJs changing with age. The blue and purple dots are the ratio of HJs with $e > 0.1$ and $e > 0.2$ changing with age, respectively. The shadow region is overplotted to emphasize the peak of the ratio.

4.2. High- e Migration of HJs around Field Stars Beyond 1 Gyr

In Figure 4, we find a tiny bump in the proportion of Jovian planets f_J around 2 Gyr, which is anticorrelated with f_{SubN} , i.e., a small dip of f_{SubN} around 2 Gyr.

High- e migration can explain the anticorrelation. During the inward migration of the Jovian planet, the inner planets can be ejected from the system due to the planet–planet interaction (Mustill et al. 2015). That is, HJs after high- e migration are usually lonely (Steffen et al. 2012; Hord et al. 2021). Thus, the proportion of smaller planets, e.g., sub-Neptunes and super-Earths, have a decl.

Due to tidal dissipation during the high- e migration, the eccentricity of the HJs will decrease with time. Therefore, if the tiny bump in the proportion of Jovian planets f_J around 2 Gyr is attributed to the HJs that form through high- e migration, we may also see a small bump in the eccentricity–age diagram around 2 Gyr.

To test this conjecture, in the following, we select 336 HJs having both eccentricity and age measurements from the NASA exoplanet archive. We constrain the period of the HJs to be shorter than 20 days, and the relative uncertainty of planet

radii is no more than 50%. Figure 5 shows the eccentricity–age distribution of the 336 HJs. In Panel (a) red dots show the median eccentricity of each age bin changing with age. The error bar is calculated according to the 16 and 84 percentiles of the eccentricities of each age bin. Because the majority of the HJs have low eccentricity, the median eccentricity of each age bin is nearly a zero constant, i.e., unchanging with age.

However, red dots have larger error bars in the older region. It seems that the number of HJs with high eccentricity increases beyond 1 Gyr. Therefore, we calculate the relative ratio of high-eccentricity HJs in each age bin, as shown in panel (b) of Figure 5. Similar to the previous analysis, this ratio is calculated with the assumption of the Gaussian distribution of age and eccentricity of each HJ. We find that both the ratio of HJs with $e > 0.1$ and $e > 0.2$ rapidly increase beyond 1 Gyr, i.e., the difference between the two data points before and after 1 Gyr is 2σ and 12σ , respectively. After reaching the maximum of around 2 Gyr, the ratio of HJs with high-eccentricity declines with age due to tidal dissipation, as expected. Therefore, the eccentricity evolution also supports the high- e migration for these HJs older than 1 Gyr.

Because HJs around field stars are the dominant population beyond 1 Gyr, as shown in Figure 2, we can conclude that the bump of f_J around 2 Gyr is likely due to the formation of HJs around field stars through high- e migration. Since the timescale of 2 Gyr is 10 times longer than the formation timescale of HJs through flyby-induced high- e migration in star clusters ($\tau_{\text{HJC}} \lesssim 200$ Myr). We explain the large differences via the different environments of stellar density. The HJs form around field stars after 1 Gyr, which escape the cluster environments at the early stage (< 100 Myr). Because the less dense dynamical environments lead to longer flyby timescale, the trigger time of high- e migration is probably much longer than that in cluster environments.

4.3. Formation of Hot Neptune Desert around 100 Myr

Several previous works found the hot Neptune desert in planetary mass–period distribution and radius–period distribution, i.e., Szabó & Kiss (2011), Beaugé & Nesvorný (2013), Mazeh et al. (2016). In Figure 4, we find that the proportion of the sub-Jupiters within 20 days, f_{SubJ} , rapidly declines around 100 Myr, then remains at the low value. The decl. is correlated to the hot Neptune desert and may indicate the formation timescale of such desert.

However, the sub-Jupiters classified via radius and period independently are not in the hot Neptune desert exactly. According to Mazeh et al. (2016), the borders of the desert are period dependent. That is, at large radii, the planet’s radius decreases with increasing period, while at small radii, the radius increases with increasing period (the dashed lines in Figure 6). Using the same region as Mazeh et al. (2016), we compare the time-dependent ratio of the number of planets inside and outside the hot Neptune desert to constrain the formation timescale of the hot Neptune desert.

In Figure 6, we show 107 planets/candidates in star clusters and 1991 other confirmed planets around field stars in the radius–period plane. We divide the planets/candidates in star clusters within 20 days into two groups. One is planets younger than 100 Myr (red circles). The other is planets older than 100 Myr (green diamonds).

We calculate the ratio of the number of planets inside and outside the hot Neptune desert, i.e., $N_{\text{in}}/N_{\text{out}}$, for both the

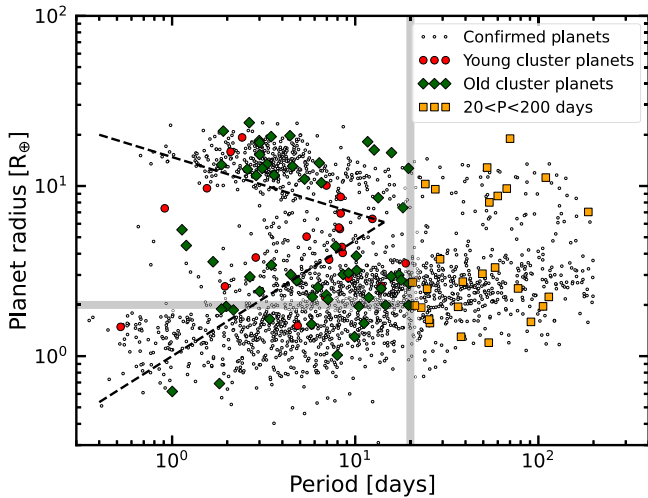


Figure 6. The scatter plot of planets in planets radius–period plane. Red dots are hot and young planets in star clusters ($P < 20$ days, age < 100 Myr). While black dots are hot and old planets in star clusters ($P < 20$ days, age > 100 Myr). Orange squares are planets in clusters with periods beyond 20 days. Two black dashed lines are boundaries of the hot Neptune desert described in Mazeh et al. (2016). The gray line of $P = 20$ days and the gray line of $R_p = 2 R_\oplus$ are overlotted for reference.

younger and older groups. Then, we use the Monte Carlo simulation to get a distribution of $N_{\text{in}}/N_{\text{out}}$ under the assumption of the Gaussian distribution of planet radius, period, and age. The error of $N_{\text{in}}/N_{\text{out}}$ is adopted according to the 16 and 84 percentiles of the ratio distribution. We find that the younger group has much higher $N_{\text{in}}/N_{\text{out}}$ ($0.80^{+0.20}_{-0.19}$) than older groups ($0.19^{+0.03}_{-0.03}$) in nearly 3.0σ confidence level. If we add a planet radius cut for detection completeness, i.e., $R_p > 2 R_\oplus$ (horizontal shadow line), the result is similar. That is, the younger group has higher $N_{\text{in}}/N_{\text{out}}$ ($0.67^{+0.17}_{-0.01}$) than the older group ($0.18^{+0.03}_{-0.01}$) in 3.67σ confidence level. Alternatively, if we use 300 Myr to distinguish the younger and older groups, the difference of $N_{\text{in}}/N_{\text{out}}$ between the young and old groups will decrease, which is smaller than the 100 Myr case. That is, the difference between the median value of the young group’s $N_{\text{in}}/N_{\text{out}}$ ($0.48^{+0.07}_{-0.05}$), and the old group’s $N_{\text{in}}/N_{\text{out}}$ ($0.31^{+0.04}_{-0.04}$). Therefore, we can conclude that the rapid decl. of f_{SubJ} around 100 Myr corresponds to the formation of the hot Neptune desert around 100 Myr.

Owen & Lai (2018) explain two boundaries of the hot Neptune desert in a combination of photoevaporation and high- e migration. For the lower boundary, photoevaporation functions effectively in the first several hundred million years and will trigger the atmospheric mass loss of Neptune-sized planets, which is consistent with the formation timescale we obtained. If the high- e migration sculpts the lower boundary, the formation timescale will be much larger than 100 Myr because the hot Neptunes usually experience longer tidal circularization ($\gtrsim 1$ Gyr). We prefer that photoevaporation sculpts the lower boundary of the hot Neptune desert around 100 Myr.

For the upper boundary, photoevaporation seems to not be a suitable explanation. Several works show that massive planets ($M_p > 0.5 M_J$) can resist photoevaporation even at extremely short periods (e.g., Owen & Jackson 2012; Tripathi et al. 2015; Owen & Alvarez 2016). Therefore, photoevaporation will predict a lower upper boundary (Figure 4 in Owen & Lai 2018). However, in some specific cases, the rapid decl.

of the radius of giant planets may explain the upper boundary of the hot Neptune desert. Exempli gratia, Thorngrén et al. (2023) developed a model including radius inflation, photoevaporative mass loss, and Roche lobe overflow, which can trigger a runaway mass loss of a puff hot Saturn around 400 Myr. Because the desert already existed around 100 Myr, we do not consider such a mechanism as the dominant.

High- e migration can deliver Jovian planets from the outer region to the inner orbit. Then, the subsequent decay due to stellar tides will further sculpt the upper boundary. More specifically, both the tidal circularization timescale (planetary tides) and tidal decay timescale (stellar tides) decrease with increasing planetary radius or mass. As described in Section 4.1, the typical formation timescale of HJs in clusters is $\lesssim 200$ Myr, which is consistent with the formation timescale of the hot Neptune desert. Therefore, flyby-induced high- e migration could sculpt the upper boundary of the hot Neptune desert in clusters.

The formation timescale of the hot Neptune desert in star clusters is around 100 Myr. When it comes to field stars, the formation timescale of the hot Neptune desert may move backward to several Gyr because of the relatively slow high- e migration for HJs around field stars. However, due to the limited sample of young planets around field stars, we do not find any evidence.

The scenario of flyby-induced high- e migration can not only explain the increment of f_j around 100 Myr, but may also sculpt the upper boundary of the hot Neptune desert around 100 Myr. Therefore, we prefer the scenario of flyby-induced high- e migration, i.e., a combination of photoevaporation and flyby-induced high- e migration could sculpt the hot Neptune desert around 100 Myr.

4.4. The Paucity of Young WJs between 100 and 1000 Myr

In the analysis above, we find that high-eccentricity migration may play an important role in the formation of HJs and the hot Neptune desert in star clusters. During the high- e migration, some progenitors of HJs (i.e., warm Jupiters and cold Jupiters) may migrate inward and become HJs. Consequently, the number of warm Jupiters and cold Jupiters may decline after ~ 100 Myr. To test the conjecture, we include warm planets in clusters within 200 days. There are seven young warm Jupiters (hereafter WJ, $20 < P < 200$ days, age < 100 Myr) in clusters, as shown in Figure 7 (green circles). However, there are no WJs in clusters with ages between 100 and 1000 Myr. This may be another hint of the flyby-induced high- e migration in star clusters.

Note there are dozens of WJs with age measurements from the NASA exoplanet archive ($20 < P < 200$ days, $8 R_\oplus < R_p < 2.5 R_J$, blue diamonds in Figure 7). The majority of these WJs around field stars are older than 1 Gyr. The absence of WJs between 100 and 1000 Myr may indicate that WJs may hardly survive in cluster environments, i.e., such relatively dense environments prefer the formation of HJs.

One should be cautious of these preliminary results; the absence of WJs between 100 and 1000 Myr may be due to the observation bias. For instance, TESS prefers to discover HJs instead of WJs because of the relatively short time span. Apart from that, the inhomogeneous age measurements from the NASA exoplanet archive may also be considered as potential observational bias. Therefore, these preliminary but intriguing results need more observation data to check.

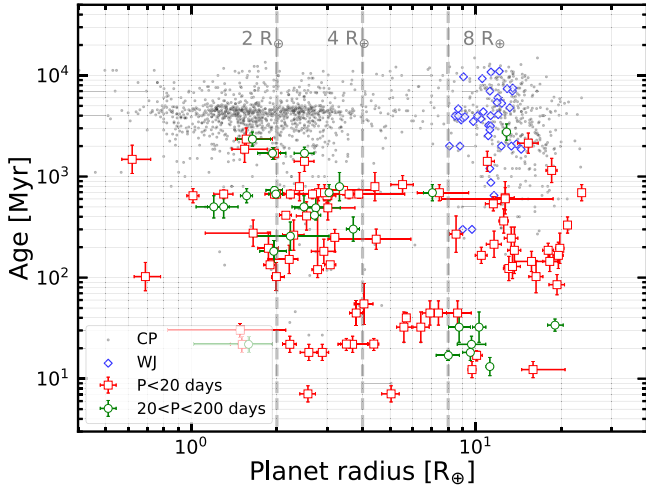


Figure 7. The planetary radius–age distribution of 107 planets/candidates (within 200 days, red squares and green circles) in clusters and 1991 confirmed planets (within 200 days, gray dots) around field stars. Here, we also show the 39 warm Jupiters around field stars with age measurements from the NASA exoplanet archive ($20 < P < 200$ days, blue diamonds).

5. Discussion

In Section 4, we have explained our statistical results through flyby-induced high- e migration and photoevaporation. However, there are still some factors that we have not discussed. In the following, we discuss the influence of the number of stars (Section 5.1) and some caveats of eccentricity measurement for young planets (Section 5.2).

5.1. The Evolution of Planet Radius Considering the Number of Stars

Note that the number of stars varies in different clusters, which may influence the occurrence of the planet to some extent. For example, Fang et al. (2023) use TESS data to constrain the HJ occurrence rate in associations. However, it is out of our concern in this paper. Therefore, we do not use the planet occurrence rate to describe the evolution of planet radius, which will be discussed further in our next paper. Here, we simply use the fraction of planets with different sizes in each cluster to describe the influence of star number of the parental clusters, i.e.,

$$F(R_p, t) = \frac{\sum N_p}{N_s} \quad (4)$$

where N_p is the number of planets in one cluster and N_s is the number of cluster member stars. Similar to the calculation of f_i , i.e., proportions of planets with different sizes and ages, we use Monte Carlo simulation to derive the proportion of fraction of planets with different sizes and ages, i.e., \hat{f}_i

$$\hat{f}_i = \frac{F_i}{F_{\text{SubN}} + F_{\text{SubJ}} + F_J}, \quad (5)$$

where F_i is the fraction of planets in star clusters with different sizes and ages, i.e., F_{SubN} , F_{SubJ} or F_J corresponding to sub-Neptunes, sub-Jupiters, and Jovian planets in Section 3.1, respectively. Figure 8 shows the results of \hat{f}_i , which is similar to Figure 3. \hat{f}_J (red diamonds) increases before 100 Myr and

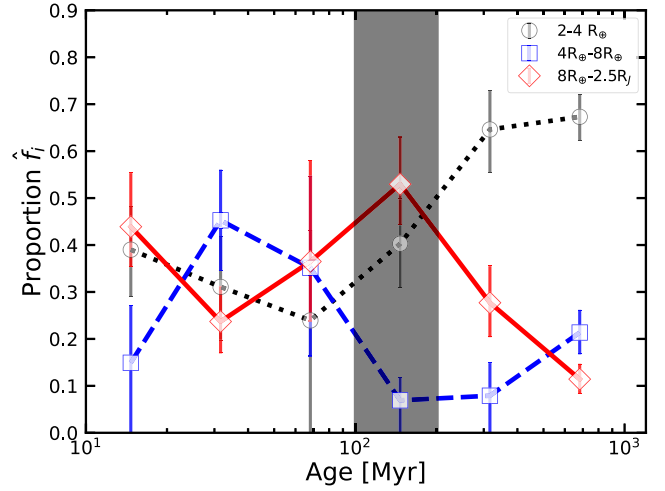


Figure 8. The time-dependent relation of the proportions of the fraction of planets of different sizes in different star clusters. Different colors show planets of different sizes. The shadow region around 100 Myr is overplotted to emphasize the typical timescale.

then declines after 200 Myr, i.e., a peak occurs between 100 and 200 Myr. \hat{f}_{SubJ} (blue squares) declines around 100 Myr. For sub-Neptunes \hat{f}_{SubN} (gray circles) shows a clear increase after 100 Myr.

5.2. Eccentricity Measurement of Young Planets

Planet eccentricity is more challenging to measure for young planets because of magnetic activity. In several cases (e.g., TOI-837 b in OC IC 2602, Bouma et al. 2020), circular orbits are simply adopted to reduce the number of parameters in the fitting.

Additionally, planets with high impact parameter b are hard to derive the accurate eccentricity distribution because of the degeneracy with other orbital parameters, e.g., $b > 0.9$ for TOI-837 b (Bouma et al. 2020).

In our sample, we exclude giant planets with orbital periods longer than 20 days. These planets may include some progenitors of HJs with highly eccentric orbits, which are going through tidal circularization and shrinking their orbit. Only including the progenitors of HJs will make the total sample more complete. However, due to the small time span of TESS, the progenitors of HJs are not detected completely. This problem will be much less sensitive for Kepler. Using high-eccentricity progenitors of HJs from Kepler data, Jackson et al. (2023) find that high-eccentricity migration is probably the dominant formation channel of HJs, yet fails to account for all of the HJs. Therefore, we emphasize that excluding progenitors of HJs will have some influence yet will not change our qualitative results of eccentricity.

6. Conclusion

Planets in young star clusters could help us understand the planet's formation and evolution because of the accurate age estimation. In Section 2, we collect the largest catalog of 73 planets and 84 candidates in star clusters by cross matching with K2020 and planets/candidates from the NASA exoplanet archive. We validate the age estimation of 70 planets/candidates in star clusters, obtain more convinced ages of three host stars via either literature or the new gyrochronological relation, and exclude eight planetary systems with no robust age estimations.

In Section 3, we use this catalog to study the planet radius–age relation. The main statistical results are as follows:

1. The proportion of Jovian planets f_J increases around 100 Myr and reaches a maximum between 100 and 200 Myr, which is mainly attributed to the HJs in star clusters. The bump of f_J around 2 Gyr is attributed to the HJs around field stars.
2. The proportion of sub-Jupiters f_{SubJ} declines rapidly around 100 Myr, then remains at a low value. The decl. of f_{SubJ} is mainly attributed to the hot sub-Jupiters in star clusters.

After discussing several possible scenarios to explain the results, we give two constraints on the hot giant exoplanet formation timescales in Section 4:

1. HJs likely form through flyby-induced high- e migration in star clusters within 200 Myr.
2. A combination of photoevaporation and flyby-induced high- e migration in star clusters can sculpt the hot Neptune desert around 100 Myr.

We find that flyby-induced high- e migration may be the dominant formation channel of HJs in star clusters. As described in Section 4.1, those HJs in star clusters will accompany an outer companion, which is an effective angular momentum transmitter during a close flyby event. Therefore, we hope to discover some outer companions beyond these HJs with the radial velocity observations from ground-based telescopes and the astrometric data from the future data release of Gaia.

Different from HJs in star clusters, HJs around field stars may have a much longer formation timescale (~ 2 Gyr), which can be attributed to the different dynamical environments (Section 4.2).

Note in this paper, we mainly focus on the ZLK mechanism to excite the high eccentricity of the inner Jovian planet. Actually, other mechanisms, such as planet–planet scattering, can trigger the high-eccentric orbit too. Wang et al. (2020) demonstrate that a very small fraction of HJs can form from the fly-induced planet–planet scattering channel, i.e., the ZLK mechanism may be the dominant scenario of eccentricity excitation. However, we could not exclude the possibility of planet–planet scattering. One way to distinguish these two mechanisms definitely is the stellar obliquity, the angle between a planet’s orbital axis and its host star’s spin axis. ZLK mechanism predicts a bimodal stellar obliquity distribution, concentrated at 40° and 140° (e.g., Fabrycky & Tremaine 2007). While the planet–planet scattering after a convergent disk migration predicts a concentration of stellar obliquity around 90° (Nagasawa & Ida 2011).

Additionally, a hint from the absence of WJs around field stars between 100 and 1000 Myr also supports the scenario of flyby-induced high- e migration (Section 4.1). However, this absence may be due to the observation bias in Section 4.4. For instance, TESS prefers to discover HJs instead of WJs because of the relatively short time span.

In the future, with the extended mission of TESS, the Earth 2.0 mission (ET2.0, Ge et al. 2022), the Chinese Space Station Telescope (CSST, Zhan 2011; Gong et al. 2019), and PLATO (Rauer et al. 2014), we hope to detect more young planets both in star clusters and around field stars. The subsequent astrometry data from Gaia and the follow-up radial velocity

observation (including the Rossiter–McLaughlin effect) from ground-based telescopes can also provide more information about warm planets and even outer companions. A larger sample of planets in clusters will benefit us to test different formation scenarios of HJs, as well as hot Neptune deserts.

Acknowledgments

We thank the anonymous referee and Prof. Dr. Bo Ma for helpful recommendations to improve the paper. This work is supported by the National Natural Science Foundation of China (grant Nos. 11973028, 11933001, 1803012, 12150009) and the National Key R&D Program of China (2019YFA0706601). We also acknowledge the science research grants from the China Manned Space Project with No. CMS-CSST-2021-B12 and CMS-CSST-2021-B09, as well as the Civil Aerospace Technology Research Project (D050105).

Software: astropy (Astropy Collaboration et al. 2013), matplotlib (Hunter 2007), pandas (McKinney 2010), Lightkurve (Lightkurve Collaboration et al. 2018).

Appendix A Signal-to-noise-ratio–Age Relation

In young clusters, stars are more active and may hide the transiting events, especially for small planets. Thus, the detection of small planets in young clusters is uncompleted. To study the selection effects, we try to derive the empirical relations between signal-to-noise ratio (S/N) and stellar age for planets of different sizes. Then, we can select suitable criteria of planet radius to cut our samples.

The calculation of S/N of a transiting planet is calculated as follows:

$$\text{SNR} = \frac{\delta n^{0.5}}{\sigma_*(t_{\text{dur}})} \quad (\text{A1})$$

where $\delta = (R_p/R_*)$ is the transit depth of the star and n is the transit number. σ_* is the stellar photometric noise. The transit duration time t_{dur} is given by:

$$t_{\text{dur}} = \frac{PR_*\sqrt{1-e^2}}{\pi a} \quad (\text{A2})$$

where P is the planet’s orbital period and a is the semimajor axis. In the calculation of S/N, we assume that host stars are solar-like (i.e., $M_* = 1 M_\odot$ and $R_* = 1 R_\odot$) and set $P = 20$ days (because most of our select planets in star clusters are within 20 days). The same as the assumption of Mulders et al. (2015) to assume that the stellar noise changes with time as a simple power law distribution:

$$\sigma_*(t) = \sigma_{\text{LC}} \left(\frac{t}{t_{\text{LC}}} \right)^{\text{ind}_{\text{CDPP}}}, \quad (\text{A3})$$

where we normalize the noise (σ_{LC}) at the period in the long cadence, 1765.5 s (t_{LC}). ind_{CDPP} is the power law index. We use Combined Differential Photometric Precision (CDPP, Christiansen et al. 2012) from Kepler DR25, which characterizes the noise level in Kepler lightcurves. Then, using the stellar kinematic age from Chen et al. (2021), we can obtain ind_{CDPP} –age relation and S/N–age relation.

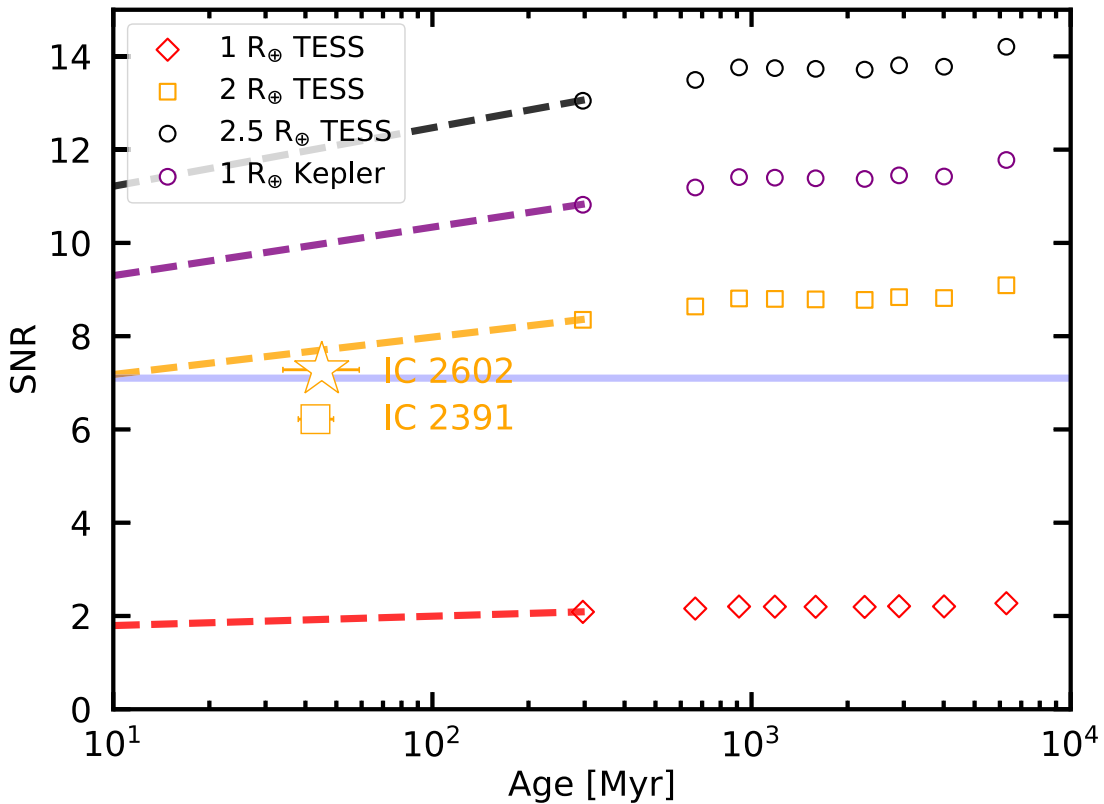


Figure A1. The S/N–age relation of planets of different sizes. Red, orange, and black hollow dots and dashed lines are S/N–age relations of planets of 1, 2, and $2.5 R_{\oplus}$ for TESS. The purple presents the S/N–age relation of planets of $1 R_{\oplus}$ for Kepler. Young open cluster IC 2602 (~ 40 Myr, orange star) and IC 2391 (~ 40 Myr, orange square) are plotted as examples. The blue horizontal line ($S/N = 7.1$) is overlotted as a reference.

For a rough calculation, we assume that the stars observed by Kepler and TESS are similar, i.e., the stellar noise evolution is similar. The major difference in the S/N of planets of different sizes lies in the observation time t_{obs} , which determines the transit numbers. Here, the observation time of the Kepler stars is ~ 1450 days, and TESS is roughly two observation sectors, i.e., ~ 54 days.

Figure A1 shows the calculated S/N of planets changing with age. Red, orange, and black hollow dots and dashed lines present the results of planets of different sizes (i.e., $1 R_{\oplus}$, $2 R_{\oplus}$, and $2.5 R_{\oplus}$) for TESS. The purple hollow dots and dashed lines show the result of planets of $1 R_{\oplus}$ for Kepler. Since the data from Chen et al. (2021) does not provide the CDPP of stars younger than 300 Myr, we simply extend the relationship to 10 Myr through a log-linear exploration. The blue horizontal line is the S/N of 7.1 above, which we consider TESS or Kepler can detect planets. To validate our empirical S/N–age relation between 10 and 300 Myr, i.e., the log-linear extrapolation, we calculate the CDPPs of the solar-type stars in two young OCs, i.e., IC 2602 (~ 40 Myr, orange star in Figure A1) and IC 2391 (~ 40 Myr, orange square). Here, the stellar noise CDPP is calculated through the simpler “sgCDPP proxy algorithm” discussed by Gilliland et al. (2011). In Figure A1, we show the median S/Ns of detecting $2 R_{\oplus}$ sized planets around solar-type stars in young OCs. The average observation

time span for these two clusters is ~ 100 days. However, to compare the log-near exploration in Figure A1, we assume that the observation time span for these two clusters is ~ 54 days. In other words, the true S/Ns of IC 2602 and IC 2391 are higher than the threshold 7.1. Thus, it is reasonable to constrain the planets above $2 R_{\oplus}$ for the estimate of completeness of transit detection. Therefore, in Section 2.2, we focus on the planets with a radius larger than $2 R_{\oplus}$ to exclude the uncompleted detection due to the stellar noise of young stars.

Appendix B Poisson Error

The “standard” confidence interval for a Poisson parameter Figure B1 shows the time-dependent relation of the proportions of planets of different sizes, adopted Poisson error. The error bar, i.e., the standard confidence interval related to a Poisson parameter, is calculated through the chi-square distribution. Panel (a) includes planets/candidates in star clusters, consistent with the results of Figure 3, although with more significant uncertainties. Panel (b) includes planets/candidates in star clusters and around field stars, consistent with the results of Figure 4. That is, the f_j increases before 100 Myr and then decreases around 1–2 Gyr.

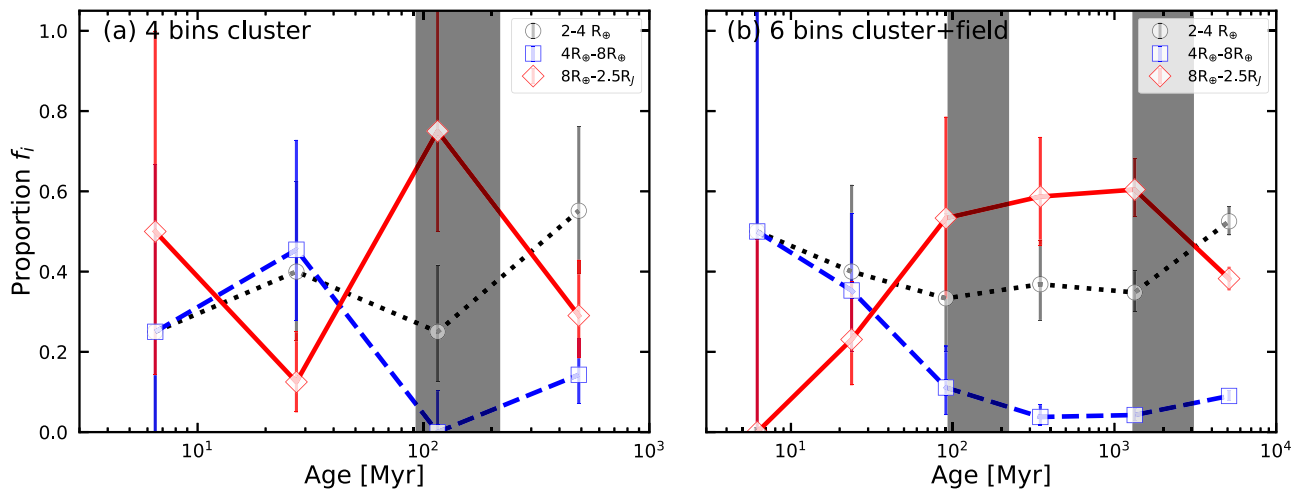


Figure B1. The time-dependent relation of the proportions of planets of different sizes. Here, the error is adopted via Poisson distribution. Panel (a) corresponds to Figure 3, and panel (b) corresponds to Figure 4.

Appendix C

The Radius Evolution of Confirmed Planets

In Figure C1, we only use confirmed planets to drive the time-dependent relation of planet radius, which is similar to that of containing planet candidates in Figure 4.

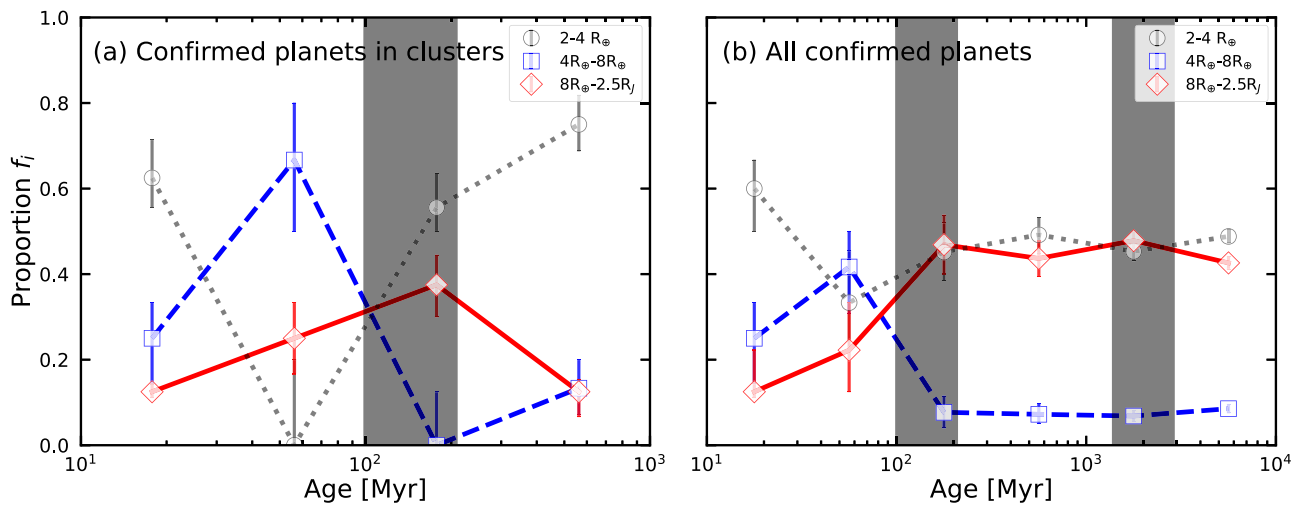


Figure C1. The time-dependent relation of the proportions of planets of different sizes. The error is adopted via MC simulation, as in Figure 3. Panel (a) uses confirmed planets in star clusters, and panel (b) uses all confirmed planets.

ORCID iDs

Yuan-Zhe Dai  <https://orcid.org/0000-0002-3401-7463>
 Hui-Gen Liu  <https://orcid.org/0000-0001-5162-1753>
 Jia-Yi Yang  <https://orcid.org/0000-0002-6332-0453>
 Ji-Lin Zhou  <https://orcid.org/0000-0003-1680-2940>

References

- Adams, F. C. 2010, *ARA&A*, 48, 47
- Anders, F., Cantat-Gaudin, T., Quadrino-Lodoso, I., et al. 2021, *A&A*, 645, L2
- Ann, H. B., Lee, S. H., Sung, H., et al. 2002, *AJ*, 123, 905
- Arancibia-Silva, J., Bouvier, J., Bayo, A., et al. 2020, *A&A*, 635, L13
- Astropy Collaboration, Robitaille, T. P., Tollerud, E. J., et al. 2013, *A&A*, 558, A33
- Barnes, S. A. 2007, *ApJ*, 669, 1167
- Beaugé, C., & Nesvorný, D. 2013, *ApJ*, 763, 12
- Berger, T. A., Huber, D., van Saders, J. L., et al. 2020, *AJ*, 159, 280
- Bouma, L. G., Curtis, J. L., Hartman, J. D., Winn, J. N., & Bakos, G. Á. 2021, *AJ*, 162, 197
- Bouma, L. G., Hartman, J. D., Bhatti, W., Winn, J. N., & Bakos, G. Á. 2019, *ApJS*, 245, 13
- Bouma, L. G., Hartman, J. D., Brahm, R., et al. 2020, *AJ*, 160, 239
- Cai, M. X., Kouwenhoven, M. B. N., Portegies Zwart, S. F., & Spurzem, R. 2017, *MNRAS*, 470, 4337
- Cantat-Gaudin, T., & Anders, F. 2020, *A&A*, 633, A99
- Cantat-Gaudin, T., Jordi, C., Vallenari, A., et al. 2018, *A&A*, 618, A93
- Carleo, I., Malavolta, L., Lanza, A. F., et al. 2020, *A&A*, 638, A5
- Chauvin, G., Lagrange, A. M., Dumas, C., et al. 2004, *A&A*, 425, L29
- Chen, D.-C., Yang, J.-Y., Xie, J.-W., et al. 2021, *AJ*, 162, 100
- Christiansen, J. L., Jenkins, J. M., Caldwell, D. A., et al. 2012, *PASP*, 124, 1279
- Craig, J., & Krumholz, M. R. 2013, *ApJ*, 769, 150
- Dai, Y.-Z., Liu, H.-G., An, D.-S., & Zhou, J.-L. 2021, *AJ*, 162, 46
- Dai, Y.-Z., Liu, H.-G., Wu, W.-B., et al. 2018, *MNRAS*, 480, 4080
- Dawson, R. I., & Johnson, J. A. 2018, *ARA&A*, 56, 175
- Fabrycky, D., & Tremaine, S. 2007, *ApJ*, 669, 1298
- Fang, Y., Ma, B., Chen, C., & Wen, Y. 2023, *Univ*, 9, 192
- Gaia Collaboration, Brown, A. G. A., Vallenari, A., et al. 2018, *A&A*, 616, A1
- Gagné, J., Faherty, J. K., Moranta, L., & Popinchalk, M. 2021, *ApJL*, 915, L29
- Gaidos, E., Mann, A. W., Rizzuto, A., et al. 2017, *MNRAS*, 464, 850
- Gan, T., Wang, S. X., Wang, S., et al. 2023, *AJ*, 165, 17
- Ge, J., Zhang, H., Zang, W., et al. 2022, arXiv:2206.06693
- Gilliland, R. L., Chaplin, W. J., Dunham, E. W., et al. 2011, *ApJS*, 197, 6
- Gong, Y., Liu, X., Cao, Y., et al. 2019, *ApJ*, 883, 203
- Hamers, A. S., & Tremaine, S. 2017, *AJ*, 154, 272
- Hardegree-Ullman, K. K., Zink, J. K., Christiansen, J. L., et al. 2020, *ApJS*, 247, 28
- Hawkins, K., Lucey, M., & Curtis, J. 2020, *MNRAS*, 496, 2422
- He, Z., Wang, K., Luo, Y., et al. 2022, *ApJS*, 262, 7
- Holl, B., Sozzetti, A., Sahlmann, J., et al. 2023, *A&A*, 674, A10
- Hord, B. J., Colón, K. D., Kostov, V., et al. 2021, *AJ*, 162, 263
- Hunter, J. D. 2007, *CSE*, 9, 90
- Itoh, Y., Hayashi, M., Tamura, M., et al. 2005, *ApJ*, 620, 984
- Jackson, J. M., Dawson, R. I., Quarles, B., & Dong, J. 2023, *AJ*, 165, 82
- Janes, K., Barnes, S. A., Meibom, S., & Hoq, S. 2014, *AJ*, 147, 139
- Johnstone, D., Hollenbach, D., & Bally, J. 1998, *ApJ*, 499, 758
- Kerr, R. M. P., Rizzuto, A. C., Kraus, A. L., & Offner, S. S. R. 2021, *ApJ*, 917, 23
- Koukel, M., & Covey, K. 2019, *AJ*, 158, 122
- Koukel, M., Covey, K., & Stassun, K. G. 2020, *AJ*, 160, 279
- Kozai, Y. 1962, *AJ*, 67, 591
- Kruijssen, J. M. D. 2012, *MNRAS*, 426, 3008
- Lada, C. J., & Lada, E. A. 2003, *ARA&A*, 41, 57
- Léger, A., Rouan, D., Schneider, J., et al. 2009, *A&A*, 506, 287
- Li, D., Mustill, A. J., & Davies, M. B. 2020, *MNRAS*, 499, 1212
- Li, D., Mustill, A. J., Davies, M. B., & Gong, Y.-X. 2023, *MNRAS*, 518, 4265
- Lidov, M. L. 1962, *P&SS*, 9, 719
- Lightcurve Collaboration, Cardoso, J. V. d. M., Hedges, C., et al. 2018
 Lightcurve: Kepler and TESS Time Series Analysis in Python, Astrophysics
 Source Code Library, ascl:1812.013
- Lindgren, L., Klioner, S. A., Hernández, J., et al. 2021, *A&A*, 649, A2
- Liu, H.-G., Zhang, H., & Zhou, J.-L. 2013, *ApJ*, 772, 142
- Lund, M. B., Rodriguez, J. E., Zhou, G., et al. 2017, *AJ*, 154, 194
- Malavolta, L., Nascimbeni, V., Piotto, G., et al. 2016, *A&A*, 588, A118
- Malmberg, D., Davies, M. B., & Heggie, D. C. 2011, *MNRAS*, 411, 859
- Mann, A. W., Gaidos, E., Mace, G. N., et al. 2016a, *ApJ*, 818, 46
- Mann, A. W., Gaidos, E., Vanderburg, A., et al. 2017, *AJ*, 153, 64
- Mann, A. W., Johnson, M. C., Vanderburg, A., et al. 2020, *AJ*, 160, 179
- Mann, A. W., Newton, E. R., Rizzuto, A. C., et al. 2016b, *AJ*, 152, 61
- Mann, A. W., Vanderburg, A., Rizzuto, A. C., et al. 2018, *AJ*, 155, 4
- Mardling, R. A. 1995a, *ApJ*, 450, 722
- Mardling, R. A. 1995b, *ApJ*, 450, 732
- Matsuyama, I., Johnstone, D., & Hartmann, L. 2003, *ApJ*, 582, 893
- Mazeh, T., Holczer, T., & Faigler, S. 2016, *A&A*, 589, A75
- McInnes, L., Healy, J., & Astels, S. 2017, *JOSS*, 2, 205
- McKinney, W. 2010, in Proc. 9th Python in Science Conf., ed. S. van der Walt & J. Millman (Austin, TX: SciPy), 56
- McQuillan, A., Mazeh, T., & Aigrain, S. 2013, *ApJL*, 775, L11
- Meibom, S., Torres, G., Fressin, F., et al. 2013, *Natur*, 499, 55
- Meingast, S., & Alves, J. 2019, *A&A*, 621, L3
- Morton, T. D., Bryson, S. T., Coughlin, J. L., et al. 2016, *ApJ*, 822, 86
- Moutou, C., Almenara, J. M., Díaz, R. F., et al. 2014, *MNRAS*, 444, 2783
- Mulders, G. D., Pascucci, I., & Apai, D. 2015, *ApJ*, 798, 112
- Mustill, A. J., Davies, M. B., & Johansen, A. 2015, *ApJ*, 808, 14
- Nagasawa, M., & Ida, S. 2011, *ApJ*, 742, 72
- Nardiello, D. 2020, *MNRAS*, 498, 5972
- Nardiello, D., Borsato, L., Piotto, G., et al. 2019, *MNRAS*, 490, 3806
- Nardiello, D., Deleuil, M., Mantovan, G., et al. 2021, *MNRAS*, 505, 3767
- Nardiello, D., Piotto, G., Deleuil, M., et al. 2020, *MNRAS*, 495, 4924
- NASA Exoplanet Science Institute 2020a, Planetary Systems Table, Version: 2023-05-16 18:35, IPAC, doi:10.26133/NEA12
- NASA Exoplanet Science Institute 2020b, Planetary Systems Composite Table, Version: 2023-05-16 18:35, IPAC, doi:10.26133/NEA13
- Neuhäuser, R., Guenther, E. W., Wuchterl, G., et al. 2005, *A&A*, 435, L13
- Newton, E. R., Mann, A. W., Kraus, A. L., et al. 2021, *AJ*, 161, 65
- Newton, E. R., Mann, A. W., Tofflemire, B. M., et al. 2019, *ApJL*, 880, L17
- Osborn, H. P., Armstrong, D. J., Adibekyan, V., et al. 2021, *MNRAS*, 502, 4842
- Owen, J. E., & Alvarez, M. A. 2016, *ApJ*, 816, 34
- Owen, J. E., & Jackson, A. P. 2012, *MNRAS*, 425, 2931
- Owen, J. E., & Lai, D. 2018, *MNRAS*, 479, 5012
- Pang, X., Tang, S.-Y., Li, Y., et al. 2022, *ApJ*, 931, 156
- Pfalzner, S., Bhandare, A., & Vincke, K. 2018, *A&A*, 610, A33
- Pfalzner, S., & Govind, A. 2021, *ApJ*, 921, 90
- Portegies Zwart, S. F., McMillan, S. L. W., & Gieles, M. 2010, *ARA&A*, 48, 431
- Rauer, H., Catala, C., Aerts, C., et al. 2014, *ExA*, 38, 249
- Rizzuto, A. C., Mann, A. W., Vanderburg, A., Kraus, A. L., & Covey, K. R. 2017, *AJ*, 154, 224
- Rizzuto, A. C., Newton, E. R., Mann, A. W., et al. 2020, *AJ*, 160, 33
- Rizzuto, A. C., Vanderburg, A., Mann, A. W., et al. 2018, *AJ*, 156, 195
- Rodet, L., Su, Y., & Lai, D. 2021, *ApJ*, 913, 104
- Roquette, J., Matt, S. P., Winter, A. J., Amard, L., & Stasevic, S. 2021, *MNRAS*, 508, 3710
- Sato, B., Izumiura, H., Toyota, E., et al. 2007, *ApJ*, 661, 527
- Spada, F., & Lanzafame, A. C. 2020, *A&A*, 636, A76
- Spurzem, R., Giersz, M., Heggie, D. C., & Lin, D. N. C. 2009, *ApJ*, 697, 458
- Stassun, K. G., Oelkers, R. J., Paegert, M., et al. 2019, *AJ*, 158, 138
- Steffen, J. H., Ragozzine, D., Fabrycky, D. C., et al. 2012, *PNAS*, 109, 7982
- Sun, L., Ioannidis, P., Gu, S., et al. 2019, *A&A*, 624, A15
- Szabó, G. M., & Kiss, L. L. 2011, *ApJL*, 727, L44
- Talens, G. J. J., Justesen, A. B., Albrecht, S., et al. 2018, *A&A*, 612, A57
- Thompson, S. E., Coughlin, J. L., Hoffman, K., et al. 2018, *ApJS*, 235, 38
- Thorngrén, D. P., Lee, E. J., & Lopez, E. D. 2023, *ApJL*, 945, L36
- Tripathi, A., Kratter, K. M., Murray-Clay, R. A., & Krumholz, M. R. 2015, *ApJ*, 808, 173
- Vanderburg, A., Mann, A. W., Rizzuto, A., et al. 2018, *AJ*, 156, 46
- Vick, M., & Lai, D. 2018, *MNRAS*, 476, 482
- von Zeipel, H. 1910, *AN*, 183, 345
- Wang, Y.-H., Leigh, N. W. C., Perna, R., & Shara, M. M. 2020, *ApJ*, 905, 136
- Wang, Y.-H., Perna, R., Leigh, N. W. C., & Shara, M. M. 2022, *MNRAS*, 509, 5253
- Winter, A. J., Clarke, C. J., Rosotti, G., et al. 2018, *MNRAS*, 478, 2700
- Winter, A. J., Kruijssen, J. M. D., Longmore, S. N., & Chevance, M. 2020, *Natur*, 586, 528
- Yee, S. W., Winn, J. N., Hartman, J. D., et al. 2023, *ApJS*, 265, 1
- Zhan, H. 2011, *SSPMA*, 41, 1441
- Zhu, W., & Dong, S. 2021, *ARA&A*, 59, 291